frontiers | Frontiers in Astronomy and Space Sciences

TYPE Original Research
PUBLISHED 25 September 2024
DOI 10.3389/fspas.2024.1427048

OPEN ACCESS

EDITED BY
Laura Colzi,
Spanish National Research Council (CSIC), Spain

REVIEWED BY
Francesco Fontani,
Osservatorio Astrofisico di Arcetri (INAF), Italy
Pooneh Nazari,
European Southern Observatory, Germany

*CORRESPONDENCE
Prasanta Gorai,
prasanta.astro@gmail.com

RECEIVED 02 May 2024
ACCEPTED 30 August 2024
PUBLISHED 25 September 2024

CITATION
Ghosh R, Das A, Gorai P, Mondal SK, Furuya K, Tanaka KEI and Shimonishi T (2024) Understanding the various evolutionary stages of the low-mass star-formation process by SO and SO_2.
Front. Astron. Space Sci. 11:1427048.
doi: 10.3389/fspas.2024.1427048

Understanding the various evolutionary stages of the low-mass star-formation process by SO and SO_2

Rana Ghosh[1,2], Ankan Das[1,3], Prasanta Gorai[4,5]*, Suman Kumar Mondal[6], Kenji Furuya[7,8], Kei E. I. Tanaka[9] and Takashi Shimonishi[10]

[1]Institute of Astronomy Space and Earth Sciences, Kolkata, West Bengal, India, [2]Indian Centre for Space Physics, Kolkata, West Bengal, India, [3]Max-Planck-Institute for extraterrestrial Physics, Garching, Germany, [4]Rosseland Centre for Solar Physics, University of Oslo, Oslo, Norway, [5]Institute of Theoretical Astrophysics, University of Oslo, Oslo, Norway, [6]S. N. Bose National Centre for Basic Sciences, Kolkata, West Bengal, India, [7]National Astronomical Observatory of Japan, Tokyo, Japan, [8]Department of Astronomy, Graduate School of Science, University of Tokyo, Tokyo, Japan, [9]Department of Earth and Planetary Sciences, Tokyo Institute of Technology, Tokyo, Japan, [10]Institute of Science and Technology, Niigata University, Niigata, Japan

SO and SO_2 are two potential candidates to trace the different evolutionary phases of the low-mass star-formation process. Here, we report observations of SO and SO_2 along with their isotopologues, ^{34}SO and $^{34}SO_2$, respectively, in four distinct phases of the low-mass star-formation process (prestellar core, first hydrostatic core, Class 0, and Class I) with an unbiased survey carried out using the Institut de Radioastronomie Millimetrique (IRAM) 30 m telescope. Interestingly, the estimated abundances of SO and SO_2 show an increasing trend from the prestellar phase to the Class 0 stage and then a decrease in the Class I phase. A similar trend is obtained for OCS and H_2S. In contrast, the obtained SO/SO_2 ratio decreases gradually from the prestellar core to the Class I stage. We have used the three-phase *Rokko* chemical code to explain our observations. The modeled abundances of SO and SO_2 exhibit an increase within the inner region as the cold gas transforms into a hot gas. The modeled abundance ratio of SO to SO_2 exhibits a notably high value in cold gas environments. This ratio decreases to less than 1 within the temperature range of 100–300 K and then increases to approximately 1 beyond 300 K. In the outer region, the simulated ratio consistently exceeds the value of 1. Our work is an observational testbed for modeling the chemistry of SO/SO_2 during low-mass star formation. However, our findings may require more sample sources with higher resolution and a more robust model for validation.

KEYWORDS

astrochemistry, interstellar medium, molecules, abundances, low-mass star formation, chemical evolution, astrochemical model

1 Introduction

Sulfur is the 10th most abundant (~10^{-5}; García-Rojas et al., 2006; Martín-Hernández et al., 2002) element in the interstellar medium (ISM) and is known to play a significant role in biological systems. Several sulfur-bearing molecules and ions have been observed in the ISM and circumstellar shells (McGuire, 2022, CDMS (https://cdms.astro.uni-koeln.de/classic/molecules)) in the Milky Way, as well as in solar nebula (Fegley Jr, 1999; Pasek et al., 2005; Mandeville, 2010), comets (Biver et al., 1997; Woodney et al., 1997), and other galaxies (Shimonishi et al., 2016; 2018; 2023). The largest sulfur-bearing molecule, ethyl mercaptan, C_2H_5SH, was recently observed in Orion (Kolesniková et al., 2014). The chemistry of interstellar sulfur is still undetermined. Only approximately 0.1% of the measured gas-phase abundance of sulfur-bearing species is found in diffuse clouds compared to dense clouds (Tieftrunk et al., 1994; Charnley, 1997; Wakelam et al., 2004; Jenkins, 2009; Vastel et al., 2018). This reduction in abundance significantly impacts the chemistry of star-forming regions (Jenkins, 2009; Rivière-Marichalar et al., 2019). Since sulfur and oxygen are chalcogens and belong to the same periodic group, their chemical properties are expected to be comparable. The lower electronegativity of sulfur relative to oxygen allows sulfur to absorb a positive charge more easily, while allowing hydrogen bonds to be created. This makes sulfur chemistry more diverse.

SO emission has been found in the disc component of Class 0/I sources and the outflow cavity walls (Sakai et al., 2014; Harsono et al., 2014; Tychoniec et al., 2021), and SO_2 is commonly seen in compact emission toward Class 0 sources and has been suggested to trace accretion shocks at the disk–envelope interface (Oya et al., 2019; Artur et al., 2022). Buckle and Fuller (2003) studied the chemical evolution of SO, SO_2, and H_2S in the low-mass star-formation process. They showed that the chemical evolution of sulfur-bearing species could be a potential indicator of the chemical timescales in the low-mass star-formation process. It has long been proposed that H_2S (Smith, 1991; Charnley, 1997; Navarro-Almaida et al., 2020) and/or Carbonyl Sulfide (OCS) (Hatchell et al., 1998; van der Tak et al., 2003) are major sulfur grain reservoirs, forming SO, SO_2, and other S-bearing molecules in the gas phase (Esplugues et al., 2014; Podio et al., 2014; Holdship et al., 2016). H_2S has not yet been found in the solid phase, although OCS and SO_2 have been detected or tentatively detected in the interstellar ices (Palumbo et al., 1995; Boogert et al., 1997; Rocha et al., 2024). In the cold molecular region, H_2S is the main sulfur reservoir (Smith, 1991; Navarro-Almaida et al., 2020), although it is still debatable in which form sulfur is locked in ice. However, SO/H_2S and SO/SO_2 are suitable molecular clocks for measuring the hot-core evolution (Smith, 1991). Gorai et al. (2017); Laas and Caselli (2019) suggested that various organo-sulfur species are found in the solid phase with lower abundances. Fuente et al. (2023) listed the 20 most abundant sulfur-bearing species, in order of decreasing abundance toward low-, intermediate-, and high-mass star-forming regions that are representative of Taurus, Perseus, and Orion A molecular clouds, respectively. In particular, theoretical work and laboratory experiments show that sulfur allotropes, such as S_8, could be an important reservoir of sulfur (Wakelam et al., 2004; Jiménez-Escobar et al., 2012; Shingledecker et al., 2020; Cazaux et al., 2022). Zhang et al. (2023) compared the distributions of sulfur-bearing molecules (SO, SO_2, ^{34}SO, and CS) and dust polarization of nine sources from the Perseus molecular cloud. This comparative analysis may offer additional diagnostics of physical properties and grain alignment mechanisms in star-forming processes, especially for the shocked regions.

Various sulfur-related molecules, including SO and SO_2 with their ^{34}S isotopologues, were observed at millimeter wavelengths by Herpin et al. (2009) in two mid-infrared quiet and two brighter massive cores with the IRAM 30 m and Caltech Submillimeter Observatory (CSO) telescopes. The study of the differences in abundance ratios between sources shows that the relative abundances of SO and SO_2 increase with time. They found that molecular ratios like SO/SO_2 may be a useful indicator of evolution, depending on the layers probed by the observed molecular transitions. An extensive statistical analysis on detection rates, emitting regions, and molecular column densities of simple sulfur-bearing molecules SO, CS, ^{34}SO, and SO_2, toward a sample of 50 Class 0/I sources in the Perseus star-forming region, was carried out by Artur et al. (2023) in the framework of the Perseus ALMA (Atacama Large Millimeter/submillimeter Array) Chemical Survey (PEACHES; Yang et al., 2021). They demonstrated that the $^{32}SO/^{34}SO$ ratio is a useful indicator of the inner high-density envelope and could be used to infer the existence of multiple COMs. Recently, Fontani et al. (2023) analyzed an observation of S-bearing molecules with the IRAM 30 m telescope toward 15 well-known cores classified in the three main evolutionary stages (high-mass starless cores, high-mass protostellar objects, and ultracompact HII regions) of the high-mass star-formation process. The molecular abundances of SO, SO_2, and H_2S exhibit the largest positive correlation with the kinetic temperature, which is thought to be an indicator of evolution.

This paper mainly focuses on the observation of SO and SO_2 in their ground state ($v = 0$) and their isotopologues toward four different stages of the low-mass star formation: prestellar core (PC, L1544), first hydrostatic cores (FHSC, B1-b), Class 0 (IRAS4A), and Class I (SVS13A) phases. Since it is not possible to observe the temporal evolution of a molecular cloud over such an astronomical period, we have used the ASAI (Astronomical Surveys At IRAM; see Section 2 for project description) data, which focus on the study of different evolutionary stages of the low-mass star-formation process. Here, we report the identification of OCS, H_2S, SO, SO_2, ^{34}SO, and $^{34}SO_2$ obtained in these four sources. We use rotational diagram analysis to estimate the excitation temperature and column density of these species. Finally, an astrochemical model is used to simulate the abundance of SO and SO_2 for different stages and to compare the simulated abundances with observed values to understand its correlation with different evolutionary stages.

This paper is organized as follows. Section 2 presents the observations and brief information about the targeted sources. Section 3 describes the method used. Results and discussion are presented in Section 4 and Section 5, respectively. Finally, we provide the conclusion in Section 6.

2 Observations and targets

We use publicly available archival data from one of the official repositories of the ASAI data at IRAM. Observations were made

with the IRAM 30 m telescope at Pico Veleta (Spain) in the framework of large program ASAI (PIs: Bertrand Lefloch and Raphael Bachiller) data using the broad-band Eight MIxer Receiver (EMIR) connected to the fast Fourier transform spectrometers (FFTSs). These observations cover three frequency bands: 3 mm (80 – 116 GHz), 2 mm (130 – 172 GHz), and 1.3 mm (200 – 276 GHz). The 3-mm observations were performed with a higher spectral resolution of 50 kHz, whereas the 1- and 2-mm observations with a spectral resolution of 200 kHz were used for these observations. The beam size or HPBW (half power beam width) of the IRAM 30 m telescope is determined by the following relation[1]: HPBW (arcsec) = 2460/frequency (GHz). The telescope HPBW lies from $\simeq 9''$ at 276 GHz to $\simeq 30''$ at 80 GHz. For a more detailed description of sensitivity achieved in each observed frequency band and other observation details, see Fuente et al. (2016); Lefloch et al. (2018). This systematic line survey covers the prestellar core, protostar, outflow region, and protoplanetary disk phase to understand the chemical and dynamical evolution of the solar-type protostar. We considered a sample of four template sources, namely, L1544, B1-b, IRAS4A, and SVS13A, covering different stages from the prestellar to the protostellar phase. The sources considered in this study are discussed in the section below.

2.1 L1544

L1544 (α_{J2000} = 05$^{\rm h}$04$^{\rm m}$17$^{\rm s}$.21, δ_{J2000} = 25°10′42″.8) is a dense starless core in the Taurus molecular cloud (TMC). It is in the early stages of star formation before collapsing (Tafalla et al., 1998). It is located at a distance of 140 pc from the Sun (Cernicharo and Guélin, 1987). Before the ALMA high angular resolution band, six continuum emission data of Caselli et al., 2019, 2022, the inner region of the prestellar core (up to a few thousand au scale) remained unexplored. They named the small dense area (~10″ ~ 1400 AU) "kernel." Matters accumulate in the core during the prestellar core phase, resulting in a decrease in the temperature and an increase in the central density (Spezzano et al., 2017). As a result, atoms and molecules freeze on the dust and form an icy grain mantle. An extremely low temperature of 7 K (Crapsi et al., 2007) is attained with a core density of 10^6 cm^{-3} (Caselli et al., 2019). Keto and Caselli (2010) found that a significant dust opacity must be taken into account for modeling to replicate the recorded temperature reduction inside 2000 AU. However, numerous sulfur-related molecules and complex organic molecules (COMs) were detected in the outer layer rather than in the dense inner cores in L1544 (Vastel et al., 2014; López-Sepulcre et al., 2015; Vastel et al., 2018). This is likely due to the non-thermal desorption, causing them to populate the gas phase under such a cold environment.

2.2 B1-b

Barnard 1 (B1) cloud is a moderately active star-forming region. It belongs to the Perseus molecular cloud complex at a distance of 235 pc (Hirota et al., 2008). The Barnard 1 dark cloud is subdivided into several dense cores, namely, B1-a, B1-b, B1-c, and B1-d. The B1-a and B1-c hosting Class 0 sources are associated with high-velocity outflows (Hatchell et al., 2005; 2007). The protostellar core B1-b consists of three remarkable sources, out of which B1-bN and B1-bS (Huang and Hirano, 2013) are two extremely young protostellar objects and are the first hydrostatic core (FHSC) candidates (Larson, 1969, first object to be formed in the collapse of a prestellar core). The spectral energy distribution (SED) modeling from Pezzuto et al. (2012) revealed that the two young protostellar objects are more evolved than prestellar cores but have yet to form Class 0 objects. Particularly, the non-detection of B1-bS at 24μm and detection at 70μm confirms that this source is at the first hydrostatic core stage. Another source, B1-bW, is observed in millimeter and sub-millimeter wavelengths (Gerin et al., 2017; Cox et al., 2018). B1-bN and B1-bS are separated from each other by approximately 18″. The targeted position (α_{J2000} = 03^{h}33^{m}20^s.8, δ_{J2000} = 31°07′34″.0) of B1-b lies in between the two FHSC candidates B1-bN and B1-bS. The two protostellar cores lie inside the HPBW of the 30-m telescope at 3 mm, but they were not resolved at 1 mm with the observations from the same survey (see Figure 1 in Fuente et al., 2016). The overall bolometric luminosity of this system is 0.77$L_\odot$ (Lefloch et al., 2018) and has a systematic velocity of 6.5 km s^{-1} (López-Sepulcre et al., 2015). Marcelino et al. (2018) observed that B1-bS shows intense and rich spectra, while B1-bN is mostly free of line emission.

2.3 IRAS4A

NGC1333-IRAS4A (or simply IRAS4A, α_{J2000} = 03^{h}29^{m}10^s.42, δ_{J2000} = 31°13′32″.2) is a protobinary system located in the NGC1333 star-forming region of the Perseus molecular cloud at a distance of 299 ± 15 pc (Zucker et al., 2018) having a systematic velocity of 7.2 km s^{-1} (Taquet et al., 2015). Interferometric measurements revealed that this binary system comprises two Class 0 objects: IRAS4A1 and IRAS4A2 separated by 1.8″ (Looney et al., 2000; López-Sepulcre et al., 2017; Tobin et al., 2018). The overall bolometric luminosity and its total envelope mass are estimated to be 9.1$L_\odot$ and 5.6$M_\odot$, respectively (Kristensen et al., 2012; Karska et al., 2013; Tobin et al., 2016). A spectacular large-scale (a few arcminutes) bipolar molecular outflow is associated with the IRAS4A system (Blake et al., 1995; Choi, 2005; Yıldız et al., 2012; Santangelo et al., 2014). IRAS4A1 is likely chemically rich, but dust optical depth does not allow us to observe the richness, as demonstrated by De Simone et al. (2020), but in IRAS4A2, numerous emissions from COMs have been identified (Bottinelli et al., 2004; 2007; Taquet et al., 2015; Santangelo et al., 2015; López-Sepulcre et al., 2017).

2.4 SVS13A

SVS13A is a Class I protostar belonging to the SVS13 cluster, located in the NGC1333 star-forming region in Perseus. The Global Astrometric Interferometer for Astrophysics, Gaia, has precisely determined its distance to be 299±14 pc (Zucker et al., 2018). The continuum observations of the SVS13 system at 82 GHz were performed in the framework of the Large Program Seeds

1 https://publicwiki.iram.es/Iram30mEfficiencies

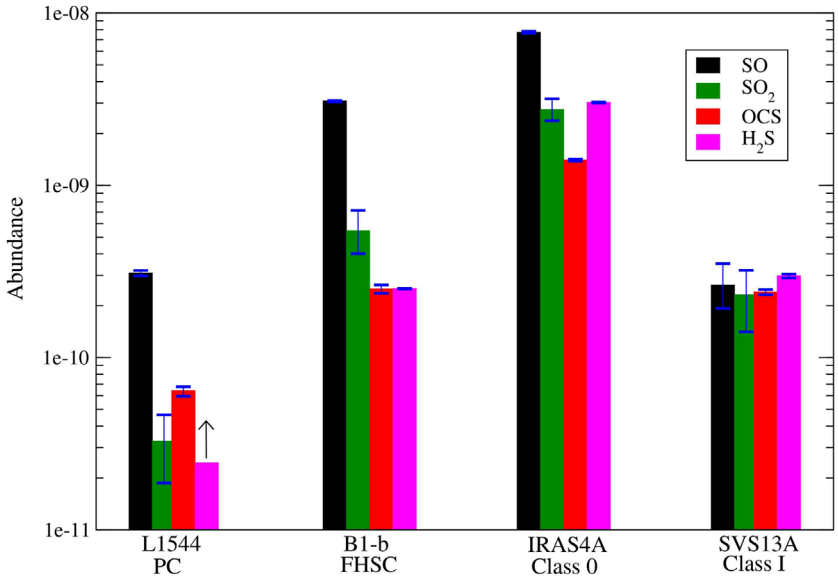

FIGURE 1
Abundance variation of SO, SO_2, OCS, and H_2S in different evolutionary stages of the low-mass star-formation process. Blue-colored cap-tipped lines represent the uncertainties in the abundance of the observed molecules. A lower limit on H_2S column density is plotted (shown in black-colored up-arrow sign) in the case of L1544, and it is taken from Vastel et al. (2018).

of Life in Space (SOLIS) using the IRAM-Northern Extended Millimeter Array (NOEMA) interferometer by Bianchi et al. (2019). They showed that this SVS13 system is mainly composed of three sources. The Class I protostar, SVS13A (α_{J2000} = $03^h29^m03^s.73$, δ_{J2000} = $31°16'03''.8$) is the brightest source in the millimeter range. SVS13B is a younger Class 0 source located ~$15''$ southeast (SE) concerning SVS13A, and there is another source, namely, SVS13C, which is located at a distance ~$20''$ to SVS13A. It is also revealed from the observation that the source SVS13A is also composed of two binary systems, VLA4A and VLA4B, with a separation of ~$0.3''$ to each other (Anglada et al., 2000; Tobin et al., 2016; 2018), and a third object VLA3 is located close (~$4''$) to the SVS13A source. From Lefloch et al. (1998), it is known that a large-scale molecular envelope surrounds these three objects. SVS13A has a luminosity (L_{bol}) of ~$32.5L_{\odot}$ (Tobin et al., 2016) with a systematic velocity of 8.6 km s^{-1} (Chen et al., 2009), and it is driving an extended molecular outflow (Lefloch et al., 1998; Codella et al., 1999; Dionatos et al., 2020) as well as younger flows moving toward SE directions (Lefèvre et al., 2017). It hosts rich chemistry, including emission from several interstellar complex organic molecules (López-Sepulcre et al., 2015; De Simone et al., 2017; Bianchi et al., 2019; Belloche et al., 2020; Codella et al., 2021; Yang et al., 2021; Diaz-Rodriguez et al., 2022; Hsieh et al., 2024).

We found that our calculated column densities for SO and ^{34}SO fall within the margin of error of the values reported in Vastel et al. (2018) and Fuente et al. (2016). However, instead of directly using those values, we prefer to reanalyze the data as we disclosed discrepancies between the data used in those papers and the data available in the public domain. For instance, in the case of L1544, Vastel et al. (2018) reported three transitions of SO, but we found only two transitions because the 109.2522 GHz transition falls outside the publicly available data range (80 – 106 GHz) [https://www.iram.fr/ILPA/LP007]. Similarly, in the case of B1-b, one transition of SO_2 at 116.98045 GHz, included in the analysis by Fuente et al. (2016), falls outside the archival dataset available at [https://www.iram.fr/ILPA/LP007], which covers the following ranges: 80.5 – 112.3 GHz, 129.9 – 172.7 GHz, and 200.5 – 276 GHz. On the other hand, increasing the sample size would enhance the robustness of the findings. However, the necessary transitions we obtained in L1544, B1-b, IRAS4A, and SVS13A were not identified in TMC-1 and L1527 to progress further. For instance, in TMC-1, only one transition of SO was detected, with no transitions observed for ^{34}SO, SO_2, H_2S, OCS, and $^{34}SO_2$ in the archival data. Similarly, in L1527, SO and SO_2 lines were detected, but no transitions of other relevant species (^{34}SO, $^{34}SO_2$, H_2S, and OCS) were found. Consequently, we cannot ascertain the variations in SO, SO_2, OCS, and H_2S abundances in TMC-1 and L1527. Hence, we excluded them from our analysis and focused only on L1544, B1-b, IRAS4A, and SVS13A.

3 Methodology

3.1 Line identification

The line identification of all observed molecular species presented in this paper was carried out with the help of CASSIS (Caux et al., 2011)[2] software (developed by IRAP-UPS/CNRS). Assuming no beam dilution, the observed line intensities (in the unit of antenna temperature, T_A^*) were transformed into the main-beam temperature (T_{mb}) by using the relation, $T_{mb} = T_A^* \times F_{eff}/B_{eff}$, where

2 https://cassis.irap.omp.eu/

F_{eff} and B_{eff} are the forward and beam efficiencies, respectively. The center frequency of a line of a given species (atom, molecule, or ion) in the laboratory is compared to the measured frequency of that species to identify a spectral line. The Cologne Database for Molecular Spectroscopy (CDMS[3]; Müller et al., 2005), which is relevant for molecular astrophysics in the regime of radio to the far-infrared, is used here to know the spectroscopic details of a molecule. In this study, we check the line blending and consider only those transitions with an intensity greater than or equal to 3σ, where σ is the RMS (root mean square) noise. Finally, we use the local thermodynamical equilibrium (LTE) modeling to confirm or reject the identification by creating synthetic spectra and comparing them with the observed profile.

3.2 Rotation diagram analysis

We applied the rotational diagram method whenever we detected multiple transitions of the same species in the same source. The analysis of rotational diagrams holds significant importance in demonstrating the essential characteristics of molecular clouds and their individual components. This method proves most effective when the source completely occupies the beam and the emitted radiation is optically thin. In LTE, all transitions are thermalized according to the Boltzmann distribution. Within the context of LTE, an optically thin transition results in an antenna temperature that is directly proportional to the column density of the observed transition's upper level.

The column density at the upper level for optically thin lines (Sutton et al., 1995; Goldsmith and Langer, 1999) can be written as

$$\frac{N_u^{thin}}{g_u} = \frac{3k_B \int T_{mb} dV}{8\pi^3 \nu S \mu^2}, \tag{1}$$

where g_u is the degeneracy of the upper state; $\int T_{mb} dV$ is the integrated intensity of the line, which was calculated from observations by doing the Gaussian fitting; k_B is the Boltzmann constant; ν is the frequencies at which the different transition occurs; S is the line strength, which is the square of the matrix elements for the direction cosines between molecular-fixed components of the dipole moment and the electric field (Yamamoto, 2017); and μ is the permanent electric dipole moment of a molecule. The total column density N_{total} is given as follows:

$$\frac{N_u^{thin}}{g_u} = \frac{N_{total}}{Q(T_{rot})} e^{-E_u/kT_{rot}}, \tag{2}$$

where $Q(T_{rot})$ is the partition function at the rotational temperature T_{rot} and E_u is the energy of the upper state. We have the final following relation after taking the log in both sides of Equation 2:

$$\log\left(\frac{N_u^{thin}}{g_u}\right) = -\left(\frac{\log e}{T_{rot}}\right)\left(\frac{E_u}{k_B}\right) + \log\left(\frac{N_{total}}{Q(T_{rot})}\right). \tag{3}$$

After using the Equation 1, from Equation 3, the column density and rotational temperature can be determined by plotting many transitions $\log(N_u^{thin}/g_u)$ against E_u/k_B and fitting data points with a straight line. The slope and the intercept of this straight line correspond to T_{rot} and N_{total}, respectively. All the spectroscopic parameters required in the above analysis are taken from the CDMS database. For the partition function, we interpolate the data given in the databases and estimate the appropriate $Q(T_{rot})$ at the derived rotational temperature. We were able to create a rotational diagram for at least one species in each source. Hence, whenever a rotational diagram was not possible, we applied the LTE model to generate synthetic spectra using the temperature derived for the particular source with the rotational diagram approach. We found good agreement between the observed and modeled spectra, considering the obtained column density and temperature along with their uncertainties, which were obtained from the rotational diagram.

4 Results

The line parameters of ^{34}SO and $^{34}SO_2$ transitions are measured by fitting a single Gaussian profile to the observed profile by the method discussed in Section 3.1. In contrast, no Gaussian fitting is done on SO and SO_2 molecules as their transitions could be optically thick ($\tau > 1$). The detected transitions of ^{34}SO and $^{34}SO_2$ and their line parameters are noted in Table 1, and we mention the transitions of SO and SO_2 for different sources in Table 2. The fitted spectra of ^{34}SO and $^{34}SO_2$ are shown in Figures 2–6.

We anticipated that at a reasonable temperature of the studied sources, the critical number density of the transitions for ^{34}SO and $^{34}SO_2$ was comparatively lower than that of the sources. This indicates that collisions occur frequently enough to maintain the populations close to their LTE values. Thus, we assume that all the transitions of ^{34}SO and $^{34}SO_2$ are optically thin and are in LTE conditions. We use the rotation diagram method discussed in Section 3.2 to analyze cloud properties from molecular line emission by plotting the column density per statistical weight of a number of molecular energy levels as a function of their energy above the ground state.

The data are indeed very well approximated by a straight line (see Figure 7), which confirms that the assumptions of LTE and optical depth (τ) $\ll 1$ are valid in the case of these two species. The rotation diagrams of ^{34}SO and $^{34}SO_2$ are shown in Figure 7. The derived temperatures and column densities are summarized in Table 3. The SO and SO_2 lines are often optically thick in star-forming regions. We have calculated the column density/abundance of SO and SO_2 for different sources. We check the ratio of $^{32}S/^{34}S$ in all sources by calculating $^{32}SO/^{34}SO$ and $^{32}SO_2/^{34}SO_2$. It is approximately 8 for L1544 and varies from 6.4 to 7.4 for B1-b and for IRAS4A; this value lies between 5.6 and 11. We observed that it is very small compared to the local ISM value (~22.5; Lodders, 2003, 24 ± 4; Yan et al., 2023), and given that no known fractionation reaction is available for sulfur, we have speculated that it might be due to the effect of the optical depth issue. Therefore, we derive the column density values of SO and SO_2 from their isotopologues by considering the $^{32}S/^{34}S$ ratio ~22.5. Table 3 refers to the obtained values of the column densities of these molecules.

3 http://cdms.astro.uni-koeln.de/classic/

10.3389/fspas.2024.1427048

TABLE 1 Observed transitions of ^{34}SO,$^{34}SO_2$, OCS, and H_2S toward the selected sources L1544, B1-b, IRAS4A, and SVS13A for which line parameters are calculated.

Species(Tag)	Source	Transition	Frequency	E_{up}	$S_{ij}\mu^2$	V_{LSR}	Peak intensity	FWHM	$\int T_{mb}dv$	rms
			(GHz)	(K)	(D^2)	(km/s)	(K)	(km/s)	(K.km/s)	(K)
^{34}SO (50,501) Klaus et al. (1996)	L1544	2_3–1_2	97.71531	9.1	6.92	6.9 (0.003)	0.212 (0.003)	0.39 (0.01)	0.09 (0.003)	0.004
	B1-b	2_2–1_1	84.41069	19.2	3.53	6.8 (0.15)	0.051 (0.003)	1.73 (0.29)	0.09 (0.02)	0.003
		2_3–1_2	97.71531	9.1	6.92	6.3 (0.002)	0.902 (0.003)	1.13 (0.01)	1.09 (0.01)	0.003
		3_2–2_1	106.74324	20.9	3.55	6.3 (0.02)	0.078 (0.002)	1.23 (0.06)	0.10 (0.01)	0.004
		3_4–2_3	135.77572	15.6	9.28	6.7 (0.002)	0.797 (0.003)	1.01 (0.01)	0.86 (0.01)	0.008
		4_3–3_2	155.50679	28.4	6.33	6.7 (0.01)	0.152 (0.003)	0.82 (0.02)	0.13 (0.01)	0.011
		4_4–3_3	168.81513	33.4	8.84	6.6 (0.01)	0.100 (0.002)	1.0 (0.03)	0.11 (0.01)	0.015
		5_4–4_3	201.84648	38.1	8.91	6.3 (0.01)	0.058 (0.002)	0.64 (0.02)	0.04 (0.003)	0.016
		5_5–4_4	211.01303	43.5	11.31	6.5 (0.01)	0.053 (0.002)	0.94 (0.03)	0.05 (0.004)	0.012
		5_6–4_5	215.83992	34.4	14.02	6.6 (0.003)	0.208 (0.002)	0.79 (0.01)	0.18 (0.003)	0.012
		6_7–5_6	256.87780	46.7	16.38	6.6 (0.01)	0.082 (0.001)	1.06 (0.02)	0.09 (0.003)	0.009
	IRAS4A	2_2–1_1	84.41069	19.2	3.53	7.7 (0.06)	0.058 (0.003)	1.61 (0.16)	0.10 (0.02)	0.006
		2_3–1_2	97.71531	9.1	6.92	7.6 (0.003)	0.599 (0.003)	1.56 (0.01)	1.00 (0.01)	0.005
		3_2–2_1	106.74324	20.9	3.56	7.5 (0.04)	0.062 (0.003)	1.70 (0.10)	0.11 (0.01)	0.004
		3_3–2_2	126.61393	25.3	6.28	6.9 (0.03)	0.054 (0.002)	1.77 (0.08)	0.10 (0.01)	0.005
		3_4–2_3	135.77572	15.6	9.28	7.9 (0.004)	0.529 (0.002)	1.50 (0.01)	0.85 (0.01)	0.009
		4_3–3_2	155.50679	28.4	6.33	7.5 (0.02)	0.080 (0.002)	1.57 (0.05)	0.13 (0.01)	0.008
		4_4–3_3	168.81513	33.4	8.84	7.6 (0.03)	0.058 (0.002)	2.08 (0.10)	0.13 (0.01)	0.009
		5_4–4_3	201.8465	38.1	8.91	7.4 (0.03)	0.063 (0.002)	1.51 (0.06)	0.10 (0.01)	0.013
		5_5–4_4	211.01303	43.5	11.31	7.6 (0.03)	0.057 (0.002)	1.28 (0.07)	0.08 (0.01)	0.011
		5_6–4_5	215.83992	34.4	14.02	7.6 (0.01)	0.195 (0.001)	1.72 (0.02)	0.36 (0.01)	0.011
		6_5–5_4	246.66347	49.9	11.39	…	…	…	…	0.011
		6_5–5_4	253.20701	55.7	13.74	7.2 (0.04)	0.033 (0.001)	1.76 (0.12)	0.06 (0.01)	0.008
		6_7–5_6	256.8778	46.7	16.38	7.5 (0.02)	0.092 (0.001)	2.16 (0.06)	0.21 (0.01)	0.009
	SVS13A	5_5–4_4	211.01303	43.5	11.31	8.7 (0.03)	0.064 (0.001)	1.60 (0.09)	0.11 (0.01)	0.009
		5_6–4_5	215.83992	34.4	14.02	8.2 (0.02)	0.114 (0.001)	1.67 (0.06)	0.20 (0.01)	0.009
		6_5–5_4	246.66347	49.9	11.39	8.5 (0.02)	0.067 (0.001)	1.51 (0.06)	0.11 (0.01)	0.012
		6_6–5_5	253.20701	55.7	13.74	8.6 (0.06)	0.046 (0.001)	1.74 (0.17)	0.09 (0.01)	0.024
		6_7–5_6	256.87780	46.7	16.38	8.4 (0.02)	0.088 (0.001)	2.00 (0.04)	0.19 (0.01)	0.008

(Continued on the following page)

10.3389/fspas.2024.1427048

TABLE 1 (*Continued*) Observed transitions of ^{34}SO,$^{34}SO_2$, OCS, and H_2S toward the selected sources L1544, B1-b, IRAS4A, and SVS13A for which line parameters are calculated.

Species(Tag)	Source	Transition	Frequency	E_{up}	$S_{ij}\mu^2$	V_{LSR}	Peak intensity	FWHM	$\int T_{mb}dv$	rms
			(GHz)	(K)	(D^2)	(km/s)	(K)	(km/s)	(K.km/s)	(K)
$^{34}SO_2$ (66,501) Belov et al. (1998)	L1544	$3_{1,3}$–$2_{0,2}$	102.03187	7.6	5.37	7.2 (0.03)	0.019 (0.003)	0.23 (0.06)	0.005 (0.002)	0.004
	B1-b	$3_{1,3}$–$2_{0,2}$	102.03188	7.6	5.37	6.6 (0.03)	0.052 (0.003)	1.13 (0.10)	0.06 (0.01)	0.003
		$5_{1,5}$–$4_{0,4}$	133.47147	15.5	8.36	6.5 (0.03)	0.059 (0.003)	0.83 (0.06)	0.05 (0.01)	0.009
		$4_{2,2}$–$4_{1,3}$	141.15876	18.7	6.09	6.2 (0.08)	0.018 (0.003)	0.78 (0.18)	0.02 (0.01)	0.017
		$3_{2,2}$–$2_{1,1}$	203.22514	15.0	4.44	6.5 (0.01)	0.050 (0.003)	0.35 (0.02)	0.02 (0.002)	0.011
	IRAS4A	$3_{1,3}$–$2_{0,2}$	102.03187	7.6	5.37	7.8 (0.11)	0.024 (0.003)	1.66 (0.29)	0.04 (0.01)	0.002
		$11_{2,10}$–$11_{1,11}$	201.3764	69.7	11.98	7.0 (0.02)	0.049 (0.003)	0.57 (0.04)	0.03 (0.003)	0.010
		$3_{2,2}$–$2_{1,1}$	203.2251	15.0	4.44	6.9 (0.03)	0.034 (0.002)	0.98 (0.08)	0.04 (0.01)	0.014
		$4_{2,2}$–$3_{1,3}$	229.85762	18.7	4.54	…	…	…	…	0.015
	SVS13A	$5_{3,3}$–$5_{2,4}$	247.44029	35.2	6.03	8.3 (0.03)	0.023 (0.003)	0.43 (0.06)	0.01 (0.003)	0.007
	L1544	7–6	85.13910	16.3	3.58	7.2 (0.01)	0.082 (0.002)	0.40 (0.01)	0.04 (0.002)	0.004
		8–7	97.30121	21.0	4.09	7.2 (0.01)	0.069 (0.002)	0.39 (0.02)	0.03 (0.002)	0.005
		7–6	85.13910	16.3	3.58	6.6 (0.01)	0.169 (0.003)	1.35 (0.03)	0.24 (0.01)	0.004
		8–7	97.30121	21.0	4.09	6.6 (0.01)	0.176 (0.003)	1.18 (0.03)	0.22 (0.01)	0.004
		9–8	109.46306	26.3	4.60	6.6 (0.01)	0.135 (0.003)	1.32 (0.04)	0.19 (0.01)	0.010
	B1-b	11–10	133.78590	38.5	5.63	6.7 (0.02)	0.095 (0.003)	1.12 (0.04)	0.11 (0.01)	0.008
		12–11	145.94681	45.5	6.14	6.6 (0.02)	0.081 (0.003)	1.00 (0.05)	0.09 (0.01)	0.007
		13–12	158.10736	53.1	6.65	6.6 (0.02)	0.072 (0.003)	1.00 (0.04)	0.08 (0.01)	0.010
		6–5	72.97678	12.3	3.07	7.2 (0.02)	0.146 (0.003)	1.75 (0.07)	0.27 (0.02)	0.007
OCS (60,503) Winton and Gordy (1970)		7–6	85.13910	16.3	3.58	7.6 (0.02)	0.202 (0.003)	2.24 (0.06)	0.48 (0.02)	0.006
		8–7	97.30121	21.0	4.09	7.6 (0.02)	0.222 (0.003)	1.96 (0.04)	0.46 (0.02)	0.007
		9–8	109.46306	26.3	4.60	7.6 (0.01)	0.229 (0.003)	2.06 (0.03)	0.50 (0.01)	0.010
		11–10	133.78590	38.5	5.63	7.4 (0.01)	0.205 (0.002)	2.08 (0.03)	0.45 (0.01)	0.010
		12–11	145.94681	45.5	6.14	7.3 (0.01)	0.199 (0.002)	1.98 (0.03)	0.42 (0.01)	0.011
		13–12	158.10736	53.1	6.65	7.4 (0.01)	0.192 (0.002)	2.13 (0.03)	0.44 (0.01)	0.007
	IRAS4A	14–13	170.26749	61.3	7.16	7.2 (0.01)	0.162 (0.002)	2.09 (0.03)	0.36 (0.01)	0.012
		17–16	206.74516	89.3	8.70	7.3 (0.01)	0.179 (0.001)	1.80 (0.02)	0.34 (0.01)	0.011
		18–17	218.90336	99.8	9.21	7.2 (0.01)	0.163 (0.001)	2.31 (0.03)	0.40 (0.01)	0.010
		19–18	231.06099	110.9	9.72	7.2 (0.01)	0.166 (0.001)	2.10 (0.03)	0.37 (0.01)	0.015
		20–19	243.21804	122.6	10.23	7.3 (0.01)	0.123 (0.001)	2.14 (0.04)	0.28 (0.01)	0.014
		21–20	255.37446	134.8	10.74	7.1 (0.01)	0.109 (0.001)	2.00 (0.04)	0.23 (0.01)	0.010

(Continued on the following page)

TABLE 1 (*Continued*) Observed transitions of ^{34}SO,$^{34}SO_2$, OCS, and H_2S toward the selected sources L1544, B1-b, IRAS4A, and SVS13A for which line parameters are calculated.

Species(Tag)	Source	Transition	Frequency	E_{up}	$S_{ij}\mu^2$	V_{LSR}	Peak intensity	FWHM	$\int T_{mb}dv$	rms
			(GHz)	(K)	(D^2)	(km/s)	(K)	(km/s)	(K.km/s)	(K)
		22–21	267.53022	147.7	11.25	7.0 (0.01)	0.138 (0.001)	1.95 (0.03)	0.29 (0.01)	0.014
	SVS13A	12–11	145.94681	45.5	6.14	8.8 (0.04)	0.062 (0.002)	2.31 (0.13)	0.15 (0.01)	0.012
		13–12	158.10736	53.1	6.65	8.5 (0.04)	0.099 (0.002)	3.09 (0.09)	0.33 (0.02)	0.012
		18–17	218.90336	99.8	9.21	8.5 (0.02)	0.167 (0.002)	3.63 (0.05)	0.65 (0.01)	0.009
		20–19	243.21804	122.6	10.23	8.6 (0.02)	0.122 (0.001)	2.58 (0.05)	0.34 (0.01)	0.022
		21–20	255.37446	134.8	10.74	8.8 (0.02)	0.116 (0.001)	3.16 (0.05)	0.39 (0.01)	0.013
H_2S 34,502 Belov et al. (1995)	B1-b	$1_{1,0}-1_{0,1}$	168.76276	27.9	4.31	6.4 (0.002)	1.377 (0.003)	1.16 (0.004)	1.70 (0.004)	0.016
	IRAS4A	$2_{2,0}-2_{1,1}$	216.71044	84.0	2.06	7.3 (0.004)	0.53 (0.002)	1.83 (0.01)	1.03 (0.01)	0.013
	SVS13A	$2_{2,0}-2_{1,1}$	216.71044	84.0	2.06	8.1 (0.02)	0.16 (0.001)	3.20 (0.06)	0.55 (0.01)	0.009

4.1 L1544

We identify two transitions of SO and one transition each of ^{34}SO, SO_2, and $^{34}SO_2$ in this source. In addition to these two transitions of SO at 86.0939 and 99.2998 GHz, Vastel et al. (2018) found another transition at 109.2522 GHz, but this transition is not available in the archival data (available between 80*and*106 GHz). They obtained a rotational temperature of 7.9 K and column density of $(7.2 \pm 3.2) \times 10^{12}$ cm^{-2} from rotational diagram analysis for SO. They varied the excitation temperature for ^{34}SO within 5–6 K and reported a column density of $(1.3 - 1.6) \times 10^{12}$ cm^{-2}. Our derived column density reported in Table 3 is within the error bar of Vastel et al. (2018).

We are unable to determine the rotational temperature and column density from the rotation diagram analysis since we do not observe multiple transitions of ^{34}SO, $^{34}SO_2$, and OCS in this source. The column densities of ^{34}SO, $^{34}SO_2$, and OCS are derived by solving Equation 2 under the assumption of LTE and optically thin condition. We calculate the column density of OCS by taking the average for those two transitions mentioned in Table 1 and it is similar to that derived by Vastel et al. (2018) ~4.1×10^{12} cm^{-2}) from rotational diagram analysis. Figure 5 shows the Gaussian fitted spectra of these two transitions. In this study, we assume that the observed molecular species emit from the same region and a rotational temperature of ~8 K (as Vastel et al., 2018 obtained for SO molecule). We observe similar spatial velocity and full width at half maxima (FWHM) of these molecules, which support our assumptions. No transition of H_2S is found in this source. Therefore, we use the 168.76276 GHz (lies outside in our used archival dataset) transition from Vastel et al. (2018) to observe the variation in this species throughout the evolutionary stages. Although Vastel et al. (2018) estimated a lower limit for the H_2S column density of 1.6×10^{12} cm^{-2}, based on a simple LTE modeling using an excitation temperature of 10 K. The derived column densities and abundances in this source are noted in Table 3.

4.2 B1-b

In this source, we observe 15, 10, 18, and 4 transitions of SO, ^{34}SO, SO_2, and $^{34}SO_2$, respectively. Loison et al. (2019) analyzed 3 mm data from existing surveys with the IRAM 30 m telescope with five dense cores (including B1-b) to verify their modeled results. In this source, they observed four optically thick transitions of SO at 86.0939, 99.2998, 100.0295, and 109.2521 GHz. Including these four transitions of SO, nine other transitions were considered by Fuente et al. (2016) as optically thin. We report two additional transitions of SO at 172.1814 and 251.8257 GHz in addition to observed transitions by Fuente et al. (2016). Loison et al. (2019) used three transitions of ^{34}SO at 84.4106, 97.7154, and 106.7433 GHz to perform the rotational diagram analysis. They obtained a rotational temperature of 6.5 ± 0.7 K. Except for the transitions at 246.6633 and 253.2070 GHz (weak in our observation), here we identify the same transitions for ^{34}SO reported by Fuente et al. (2016). We did not consider them in our analysis as they have low intensity (20 – 25 mK) as compared to the other observed lines (52 – 220 mK). A rotational temperature of ~8 K and column density of ~1.1×10^{13} cm^{-2} are obtained for ^{34}SO in our case. However, if we include these two weak transitions of ^{34}SO in the rotational diagram analysis, we observe a minor deviation from our present values of column density and excitation temperature.

In the case of SO_2, we observe the same transitions as reported by Fuente et al. (2016), except the transition at 116.9804 GHz, which is not available in the archival data (available between 80.5*and*112.3, 129.9*and*172.7, and 200.5*and*276 GHz). A column density of ~2.0×10^{12} cm^{-2} for $^{34}SO_2$ is

10.3389/fspas.2024.1427048

TABLE 2 Observed other transitions of SO and SO_2 toward these selected sources L1544, B1-b, IRAS4A, and SVS13A.

Species	Tag (database)	Source	Quantum no.	Frequency (GHz)	E_{up} (K)	$S_{ij}\mu^2$ (D^2)
SO, $v = 0$ Bogey et al. (1997)	48,501 (CDMS)	L1544	2_2–1_1	86.09395	19.3	3.53
			2_3–1_2	99.29987	9.2	6.91
		B1-b	2_2–1_1	86.09395	19.3	3.53
			2_3–1_2	99.29987	9.2	6.91
			5_4–4_4	100.02964	38.6	0.84
			3_2–2_1	109.25222	21.1	3.56
			3_4–2_3	138.17860	15.8	9.28
			4_3–3_2	158.97181	28.7	6.34
			4_4–3_3	172.18140	33.8	8.84
			5_4–4_3	206.17600	38.6	8.91
			5_5–4_4	215.22065	44.1	11.31
			5_6–4_5	219.94944	35.0	14.02
			2_1–1_2	236.45229	15.8	0.03
			3_2–2_3	246.40458	21.1	0.03
			6_5–5_4	251.82577	50.7	11.39
			6_7–5_6	261.84372	47.6	16.38
			4_3–3_4	267.19774	28.7	0.02
		B1-b	2_2–1_1	86.09395	19.3	3.53
			2_3–1_2	99.29987	9.2	6.91
			5_4–4_4	100.02964	38.6	0.84
			3_2–2_1	109.25222	21.1	3.56
			3_3–2_2	129.13892	25.5	6.28
			6_5–5_5	136.6348	50.7	0.65
			3_4–2_3	138.17860	15.9	9.28
			4_3–3_2	158.97181	28.7	6.34
		IRAS4A	4_4–3_3	172.18140	33.	8.84
			5_4–4_3	206.17600	38.6	8.91
			5_5–4_4	215.22065	44.1	11.31
			5_6–4_5	219.94944	35.0	14.02
			2_1–1_2	236.45229	15.8	0.03
			3_2–2_3	246.40459	21.1	0.03
			6_5–5_4	251.82577	50.7	11.39
			6_6–5_5	258.25582	56.5	13.74

(Continued on the following page)

10.3389/fspas.2024.1427048

TABLE 2 (*Continued*) Observed other transitions of SO and SO_2 toward these selected sources L1544, B1-b, IRAS4A, and SVS13A.

Species	Tag (database)	Source	Quantum no.	Frequency (GHz)	E_{up}(K)	$S_{ij}\mu^2(D^2)$
		SVS13A	6_7–5_6	261.84372	47.6	16.38
			3_3–2_2	129.13892	25.5	6.28
			5_4–4_3	206.17600	38.6	8.91
			6_5–5_4	251.82577	50.7	11.39
			6_6–5_5	258.25582	56.50	13.8
		L1544	$3_{1,3}$–$2_{0,2}$	104.02941	7.7	5.37
			$8_{1,7}$–$8_{0,8}$	83.68809	36.7	17.01
			$2_{2,0}$–$3_{1,3}$	100.87811	12.6	0.43
			$3_{1,3}$–$2_{0,2}$	104.02941	7.7	5.37
			$10_{1,9}$–$10_{0,10}$	104.23929	54.7	17.87
			$5_{1,5}$–$4_{0,4}$	135.69602	15.7	8.35
			$6_{2,4}$–$6_{1,5}$	140.30617	29.2	10.22
			$4_{2,2}$–$4_{1,3}$	146.60552	19.0	6.06
			$2_{2,0}$–$2_{1,1}$	151.37863	12.6	2.32
		B1-b	$3_{2,2}$–$3_{1,3}$	158.19974	15.3	3.85
			$10_{0,10}$–$9_{1,9}$	160.82788	49.7	17.15
			$5_{2,4}$–$5_{1,5}$	165.14465	23.6	6.55
SO_2, $v = 0$ Müller et al. (2005)	64,502 (CDMS)		$7_{1,7}$–$6_{0,6}$	165.22545	27.1	11.81
			$3_{2,2}$–$2_{1,1}$	208.70033	15.3	4.45
			$4_{2,2}$–$3_{1,3}$	235.15171	19.0	4.57
			$5_{2,4}$–$4_{1,3}$	241.61579	23.6	5.67
			$6_{3,3}$–$6_{2,4}$	254.28053	41.4	7.72
			$4_{3,1}$–$4_{2,2}$	255.55330	31.3	4.30
			$3_{3,1}$–$3_{2,2}$	255.95804	27.6	2.38
			$5_{3,3}$–$5_{2,4}$	256.24694	35.9	6.03
			$7_{2,6}$–$6_{1,5}$	271.52901	35.5	7.13
SO_2, $v = 0$			$6_{0,6}$–$5_{1,5}$	72.75824	19.15	8.03
			$8_{1,7}$–$8_{0,8}$	83.68809	36.72	17.01
			$3_{1,3}$–$2_{0,2}$	104.02941	7.74	5.37
			$10_{1,9}$–$10_{0,10}$	104.23929	54.71	17.87
			$10_{2,8}$–$10_{1,9}$	129.51481	60.93	20.78

(Continued on the following page)

10.3389/fspas.2024.1427048

TABLE 2 (*Continued*) Observed other transitions of SO and SO_2 toward these selected sources L1544, B1-b, IRAS4A, and SVS13A.

Species	Tag (Database)	Source	Quantum No.	Frequency (GHz)	E_{up}(K)	$S_{ij}\mu^2(D^2)$
			$12_{1,11}-12_{0,12}$	131.01486	76.41	17.72
			$14_{2,12}-14_{1,13}$	132.74486	108.12	31.24
			$8_{2,6}-8_{1,7}$	134.00486	43.15	15.18
			$5_{1,5}-4_{0,4}$	135.69602	15.66	8.35
			$6_{2,4}-6_{1,5}$	140.30617	29.20	10.22
			$4_{2,2}-4_{1,3}$	146.60552	19.03	6.06
			$2_{2,0}-2_{1,1}$	151.37863	12.59	2.32
			$3_{2,2}-3_{1,3}$	158.19974	15.34	3.85
			$10_{0,10}-9_{1,9}$	160.8279	49.71	17.15
		IRAS4A	$5_{2,4}-5_{1,5}$	165.14465	23.59	6.55
			$16_{1,15}-16_{0,16}$	200.8092	130.66	16.44
			$12_{0,12}-11_{1,11}$	203.3915	70.12	22.48
			$3_{2,2}-2_{1,1}$	208.70033	15.34	4.45
			$11_{1,11}-10_{0,10}$	221.96521	60.36	20.57
			$4_{2,2}-3_{1,3}$	235.15171	19.03	4.57
			$5_{2,4}-4_{1,3}$	241.61579	23.59	5.67
			$10_{3,7}-10_{2,8}$	245.56342	72.71	14.51
			$13_{1,13}-12_{0,12}$	251.19970	82.18	25.69
			$6_{3,3}-6_{2,4}$	254.2805	41.40	7.72
			$4_{3,1}-4_{2,2}$	255.55330	31.29	4.30
			$3_{3,1}-3_{2,2}$	255.95804	27.62	2.38
			$5_{3,3}-5_{2,4}$	256.24690	35.89	6.03
			$7_{3,5}-7_{2,6}$	257.09996	47.84	9.27
			$6_{3,3}-6_{2,4}$	254.28050	41.40	7.72
			$7_{2,6}-6_{1,5}$	271.52901	35.50	7.13
	64502 (CDMS)		$10_{1,9}-10_{0,10}$	104.23929	54.71	17.87
			$12_{2,10}-12_{1,11}$	128.60513	82.58	26.41
			$10_{2,8}-10_{1,9}$	129.51481	60.93	20.78
			$12_{1,11}-12_{0,12}$	131.01486	76.41	17.72
			$14_{2,12}-14_{1,13}$	132.74486	108.12	31.24
			$8_{2,6}-8_{1,7}$	134.00486	43.15	15.18
			$16_{2,14}-16_{1,15}$	143.05711	137.53	34.60

(Continued on the following page)

TABLE 2 (*Continued*) Observed other transitions of SO and SO_2 toward these selected sources L1544, B1-b, IRAS4A, and SVS13A.

Species	Tag (Database)	Source	Quantum No.	Frequency (GHz)	E_{up}(K)	$S_{ij}\mu^2(D^2)$
			$10_{0,10}-9_{1,9}$	160.82788	49.7	17.15
			$12_{0,12}-11_{1,11}$	203.39155	70.12	22.48
			$11_{2,10}-11_{1,11}$	205.30057	70.21	12.14
			$16_{3,13}-16_{2,14}$	214.68939	147.83	28.37
			$11_{1,1}1-10_{0,10}$	221.96521	60.36	20.56
			$13_{2,12}-13_{1,13}$	225.15370	92.98	13.26
			$11_{5,7}-12_{4,8}$	229.34763	122.01	3.13
			$12_{3,9}-12_{2,10}$	237.06883	93.96	18.40
			$14_{0,14}-13_{1,13}$	244.2542	93.90	28.02
			$10_{3,7}-10_{2,8}$	245.56342	72.71	14.51
		SVS13A	$15_{2,14}-15_{1,15}$	248.0574	119.33	14.06
			$13_{1,13}-12_{0,12}$	251.19967	82.18	25.69
			$8_{3,5}-8_{2,6}$	251.2106	55.20	11.03
			$6_{3,3}-6_{2,4}$	254.28053	41.40	7.72
			$4_{3,1}-4_{2,2}$	255.553302	31.29	4.30
			$3_{3,1}-3_{2,2}$	255.95804	27.62	2.38
			$5_{3,3}-5_{2,4}$	256.24694	35.88	6.03
			$7_{3,5}-7_{2,6}$	257.09996	47.84	9.27
			$9_{3,7}-9_{2,8}$	258.94219	63.47	12.39
			$11_{3,9}-11_{2,1}0$	262.25690	82.80	15.43

derived from rotational diagram analysis in our work, while Fuente et al. (2016) derived a value of 1.1×10^{12} cm^{-2} by taking into account the same transitions as us. We identify a total of six transitions of OCS in this source, and by performing RD analysis, we derive an excitation temperature of 14.5 K and a column density of $\sim2\times10^{13}$ cm^{-2} for this species. The observed transitions of OCS are shown in Figure 6. In the case of H_2S, we observe two transitions at 168.76276 and 216.71044 GHz, but we estimate the column density based on the former transition (see Figure 5) because the 216.71044 GHz transition depicts an absorption-like profile.

4.3 IRAS4A

A total of 17 transitions of SO (out of which 15 are unblended and two are blended at 129.1389 GHz with $HOCH_2CN$ and 258.2558 GHz with c-C_3H_2) with upper state energies between 9*and*57 K are observed. We observe a total of 30 transitions of SO_2 in this source, out of which the transitions at 132.7448 and 254.2805 GHz are blended with CH_3COCH_3 and H_2COH^+, respectively. In the case of ^{34}SO, we observe 13 transitions. Among them, the transitions at 246.6634 GHz may be blended slightly with C_2H_5OH. The rotational diagram analysis yields a rotational temperature of ~10 K and a column density of $\sim1.0\times10^{13}$ cm^{-2} excluding this transition. Four transitions of $^{34}SO_2$ are observed in this source. The transition at 229.8576 GHz is found to be blended with C_2H_3CN and CH_2DOH. The rotational diagram analysis is performed excluding this transition and yields a rotational temperature of ~39 K and column density of $\sim(3.5\pm0.5)\times10^{12}$ cm^{-2}. Here, we observe a total of 14 transitions of OCS having an energy range of 12–148 K. We obtain an excitation temperature of 48 K and a column density of $\sim4.2\times10^{13}$ cm^{-2} for this molecule. The observed OCS transitions are shown in Figure 6. We observe two transitions of H_2S at 168.76276 and

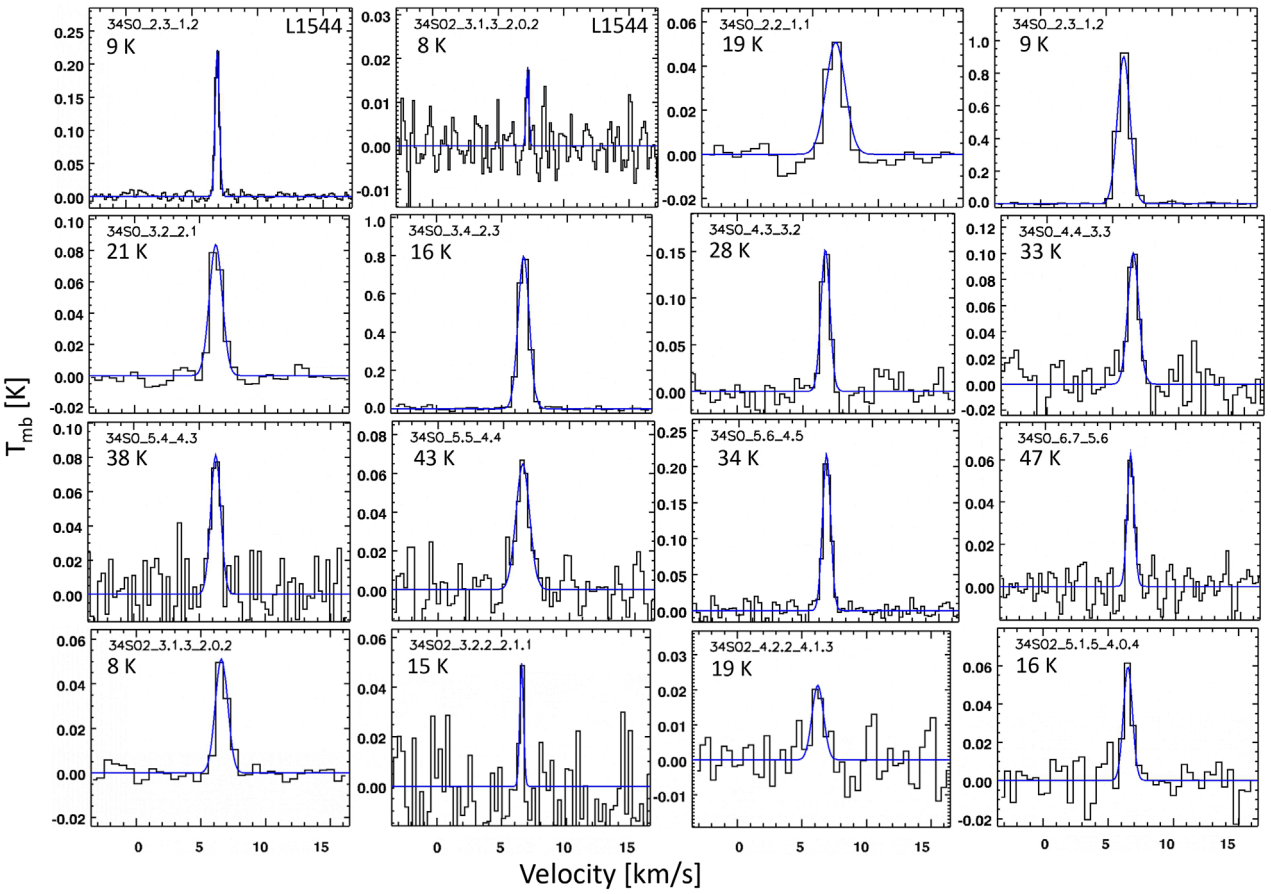

FIGURE 2
Observed transitions of ^{34}SO and $^{34}SO_2$ toward L1544 and B1-b. The top two figures are for L1544, and the rest are for B1-b. The black-colored histogram represents the observed spectra, while the Gaussian-fitted spectra are shown with blue-colored lines. The upper state energy E_{up} (in the unit of K) corresponding to each of the transitions is mentioned in each panel.

216.71044 GHz in this source. We use Equation 2 to calculate the column density of this species based only on the 216.71044 GHz transition (see Figure 5), as the other transition has an absorption-like profile.

Taquet et al. (2020) performed interferometric data analysis of IRAS4A within the framework of the SOLIS program (Ceccarelli et al., 2017). They compared interferometry results with single-dish results (ASAI) at EMIR and smoothed over the wide-band receiver (WIDEX) resolution for different sulfur-bearing species. They discussed the various line features (narrow, broad, and moderately broad), including possible physical reasons for their origin (also see Ospina-Zamudio et al., 2018).

4.4 SVS13A

We observed four transitions of SO (among them, the transition at 129.1389 GHz is blended with $HOCH_2CN$ and the 258.2558 GHz transition is blended with c-C_3H_2), five unblended transitions of its isotopologue ^{34}SO, 27 transitions of SO_2 (out which six transitions are blended with different molecules), and only one clean transition of $^{34}SO_2$ is observed in this source. Table 1 lists the detected transitions and the line parameters. We observe all ^{34}SO transitions in the 1-mm band having upper state energy 34 – 56 K and peak velocity close to the systematic velocity of the source (8.1 – 8.7 km.s^{-1}). We identify a few inverse P Cygni profiles of SO and SO_2 in this source, which are not discussed here. We use Equation 2 to derive the column density of $^{34}SO_2$ and H_2S (based on 216.71044 GHz transition; see Figure 10) by assuming an excitation temperature of 80 K (Bianchi et al., 2019). The rotational diagram of the OCS molecule in this source shows that the data points are scattered over the fitted line, i.e., the data points are not well-fitted over the line, and hence, we get a higher value of excitation temperature of approximately 200 K for this molecule. Figure 6 shows the observed spectra of OCS in this source.

Codella et al. (2021) used 3-mm and 1-mm data of NGC1333 SVS13A obtained with the IRAM-NOEMA interferometer in the framework of the SOLIS Large Program. They presented the spatial distribution on the ≤ 300 au scale of the line emission of SO, ^{34}SO, and some other S-bearing species. Furthermore, they compared their results with the ASAI data of SO, SO_2, and H_2CS and concluded that the contribution of the SO emission from the extended region

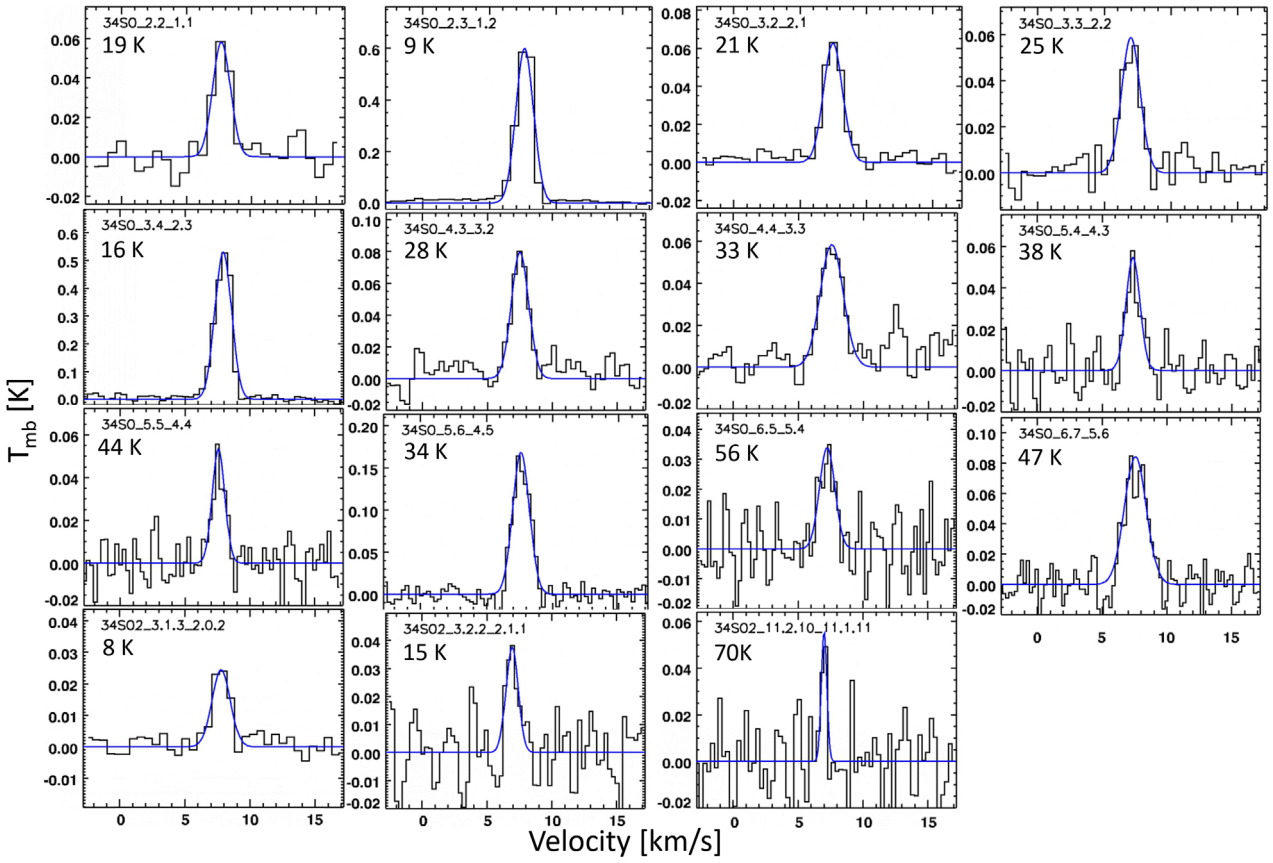

FIGURE 3
Observed transitions of ^{34}SO and $^{34}SO_2$ toward IRAS4A. The black-colored lines represent the observed spectra, while the Gaussian-fitted spectra are shown with blue-colored lines. The upper state energy E_{up} (in the unit of K) corresponding to each of the transitions is mentioned in each panel. The ^{34}SO (6_5–5_4) transition is blending with ethanol.

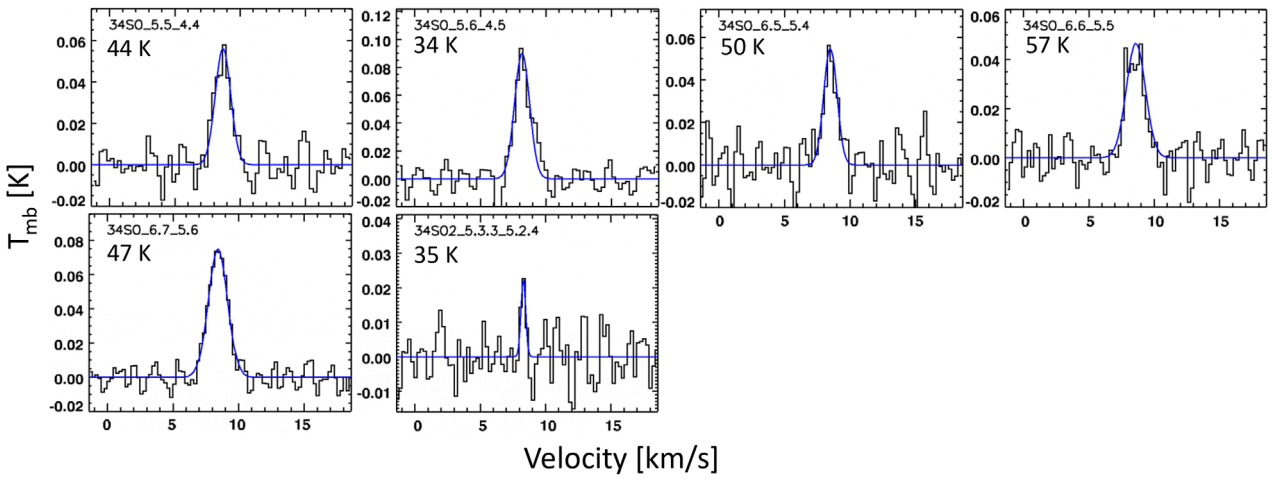

FIGURE 4
Observed transitions of ^{34}SO toward SVS13A. The black-colored lines represent the observed spectra, while the Gaussian-fitted spectra are shown with blue-colored lines. The upper state energy E_{up} (in the unit of K) corresponding to each of the transitions is mentioned in each panel.

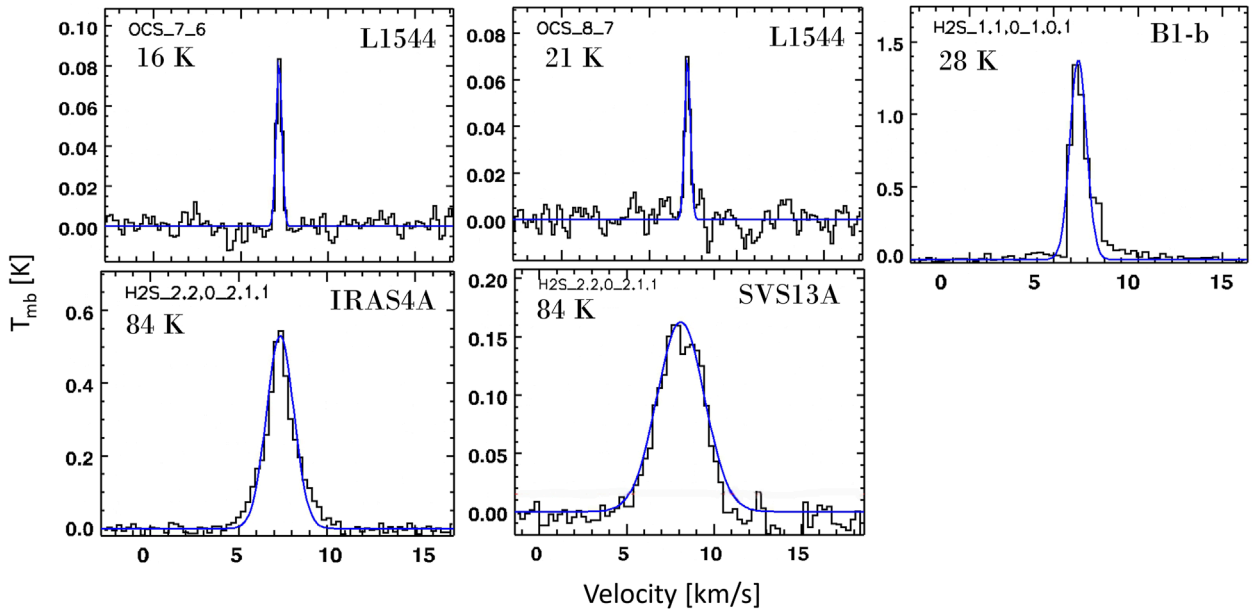

FIGURE 5
Observed transitions of OCS toward L1544 and H_2S toward B1-b, IRAS4A, and SVS13A. The black-colored lines represent the observed spectra, while the Gaussian-fitted spectra are shown in blue-colored lines. The upper state energy E_{up} (in the unit of K) corresponding to each of the transitions is mentioned in each panel.

is considerable, whereas SO_2 and H_2CS are less affected by the emission filtering.

5 Discussion

5.1 Observed abundance of SO and SO_2 and their ratio

Figure 1 illustrates the abundance variation of SO and SO_2, derived from the ^{34}S isotopologues by assuming the $^{32}S/^{34}S$ elemental ratio of 22.5 (Lodders, 2003) in four distinct phases of the low-mass star-formation process. We observe the abundance of all species initially low in the prestellar phase (L1544), then increases at the first hydrostatic core stage (B1-b), and reaches a maximum value at the Class 0 hot corino stage (IRAS4A). It decreased slightly in the further evolved Class I stage (i.e., SVS13A). We assume the excitation temperature of 8 K (for ^{34}SO and $^{34}SO_2$) for L1544 and 80 K (for $^{34}SO_2$) for SVS13A to calculate the abundance of these species. The abundances of SO and SO_2 show a similar trend when the excitation temperature is changed from 6 to 10 K for L1544 and from 60 to 100 K for SVS13A. Figure 1 depicts a similar trend for the other two major sulfur-bearing species: OCS and H_2S.

Figure 8 shows the obtained SO/SO_2 ratio for the four sources. The ratio decreases gradually from the prestellar core phase to the Class 0 phase. In the case of SVS13A, we obtain a large uncertainty in this ratio, so it is challenging to distinguish between the Class 0 and Class I source based on the SO/SO_2 ratio obtained from this observation. However, it is worth pointing out that we obtain an SO/SO_2 ratio $>$ 1 for all the stages from this observation.

5.2 Comparison with the other study

Very recently, Bhat et al. (2023) used similar sources to understand the evolutionary sequence of the low-mass star-formation process with complex organic molecules. They also found a similar trend with the COMs as it is obtained for SO and SO_2 here. A similar type of work is reported by Buckle and Fuller (2003), where they surveyed sulfur-bearing species (H_2S, SO, and SO_2) for 10 Class 0 and nine Class I sources with the 12 m telescope on Kitt Peak at National Radio Astronomy Observatory (NRAO). They reported a slight decrease in the abundance in the Class I source compared to the Class 0 source. They obtained the mean fractional abundances toward the core approximately $\sim 3.1 \times 10^{-9}$ and $\sim 7.1 \times 10^{-10}$ for SO, $\sim 4.1 \times 10^{-10}$ and $\sim 3.0 \times 10^{-10}$ for SO_2 in Class 0 and Class I source, respectively. A similar variation in the abundance of SO and SO_2 in Class 0 and Class I sources is also reported in their work. Another work on single-dish line observations of the envelopes around a sample of 18 low-mass prestellar and protostellar objects was carried out by Jørgensen et al. (2004) and reported an average abundance of $\sim 1.5 \times 10^{-9}$, $2.0 \times 10^{-9,}$ and 2.3×10^{-9} for SO in prestellar, Class 0, and Class I stage. They also found a similar variation over the prestellar phase to Class I stage.

Recently, Fontani et al. (2023) analyzed data from the IRAM 30 m telescope, focusing on 15 cores categorized into three primary evolutionary stages of the high-mass star-formation process: high-mass starless cores (HMSC), high-mass protostellar objects (HMPO), and ultracompact H II (UCHII) regions. Their findings indicated an increase in the abundance of SO and SO_2 with the evolutionary stages. Additionally, they observed a positive correlation of SO and SO_2 with the gas kinetic temperature (T_k), dust temperature (T_{dust}), luminosity (L), and luminosity-to-mass

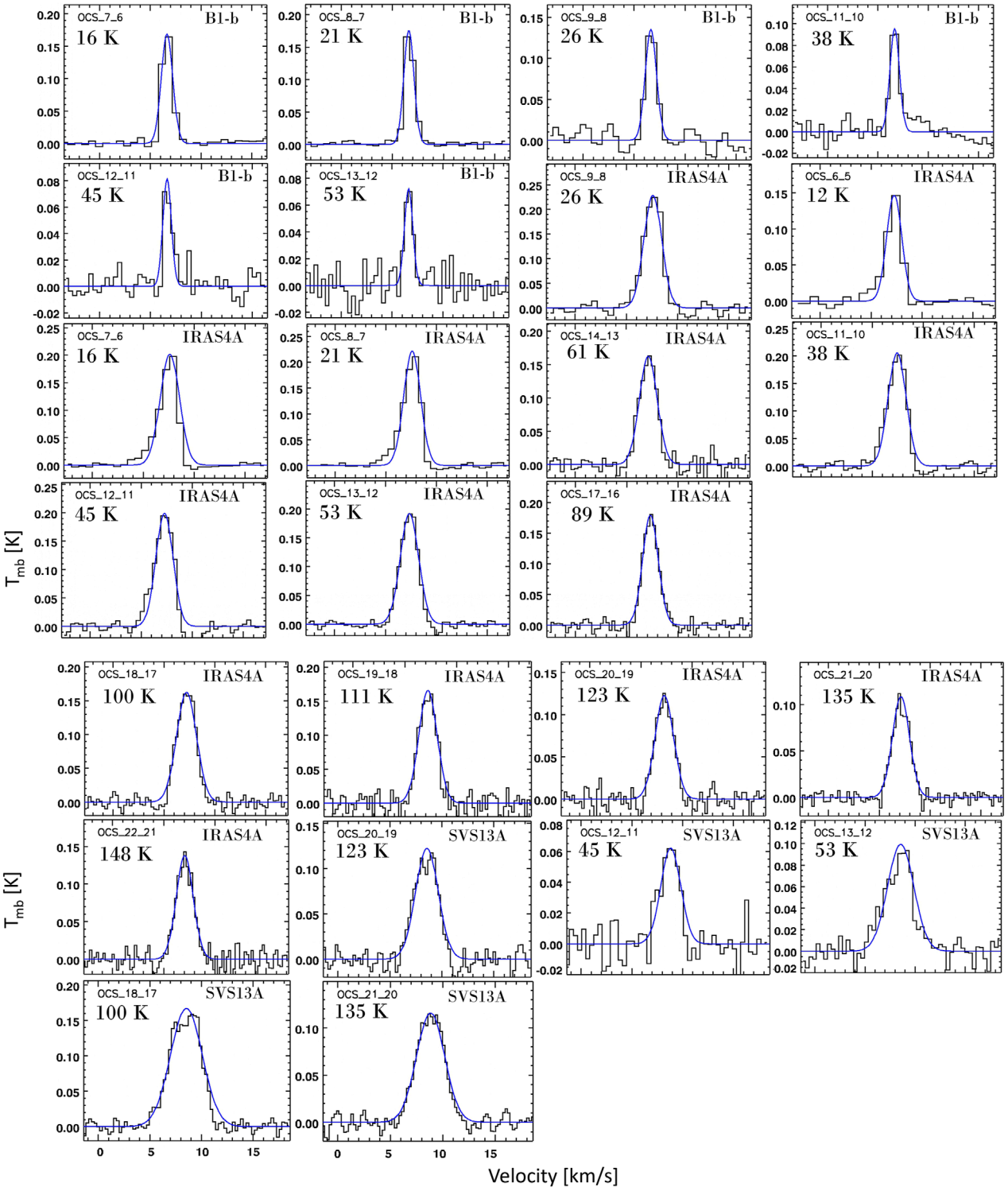

FIGURE 6
Observed transitions of OCS toward B1-b, IRAS4A, and SVS13A. The black-colored lines represent the observed spectra, while the Gaussian-fitted spectra are shown with blue-colored lines. The upper state energy E_{up} (in the unit of K) corresponding to each of the transitions is mentioned in each panel.

ratio (L/M). Similar trends were obtained for the evolutionary stages of the low-mass star-forming regions with our analysis. However, they did not find a tangible trend for the SO/SO_2 ratio with the evolutionary stages. Initially, they observed an increasing trend for SO/SO_2 during the transition from cold HMSC to warm HMSC. For HMPO and UCHII, a comparative decrease was noted compared

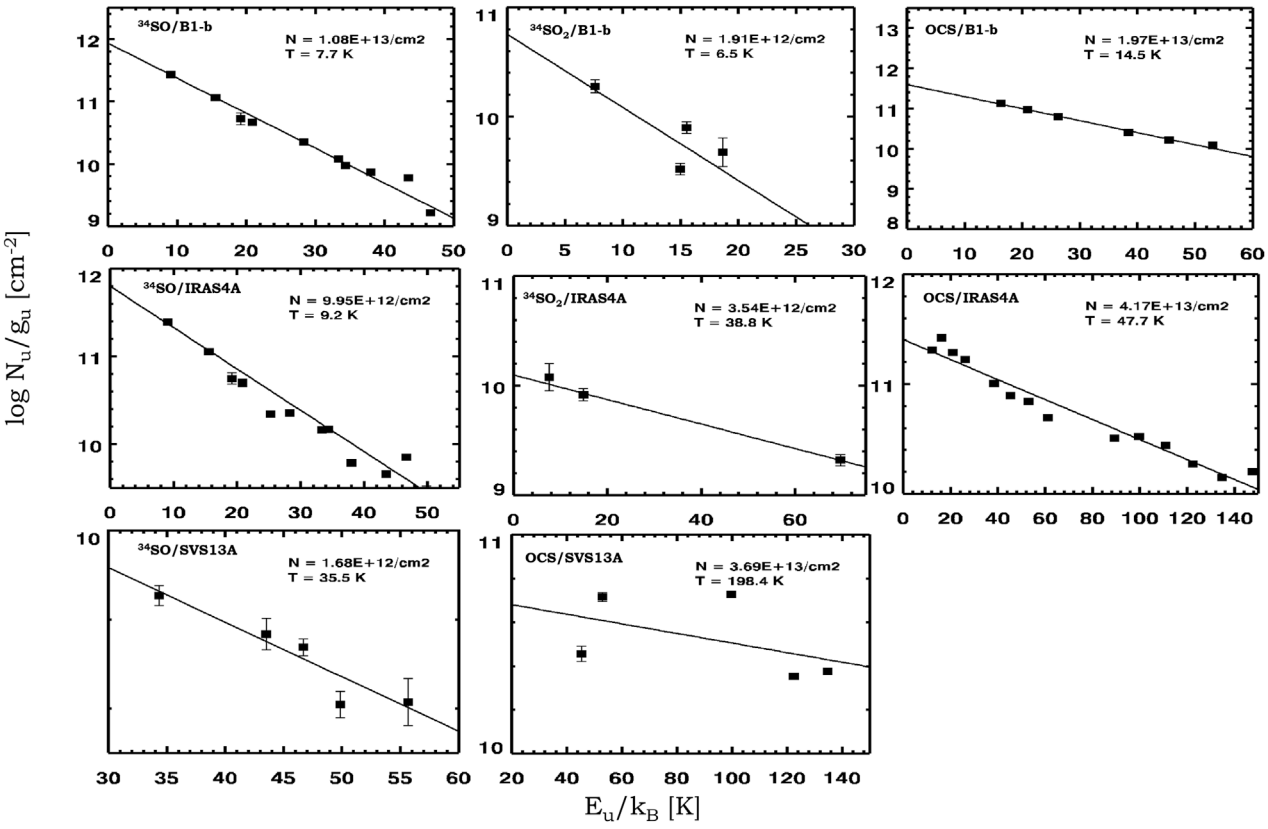

FIGURE 7
Rotational diagram for ^{34}SO, $^{34}SO_2$, OCS, and H_2S molecules in all sources, wherever it is possible to perform.

to the HMSC stages. However, they did find that the SO/SO_2 ratio consistently exceeded 1. Furthermore, Herpin et al. (2009) observed two mid-infrared quiet and two brighter massive cores. They determined that for cold outer regions (approximately 60 K), the SO/SO_2 ratio increases with the evolutionary stages. However, a definitive trend for the inner region could not be established based on their observations, whereas Wakelam et al. (2011) proposed that this ratio decreases with time in massive cores. Based on the low-energy transitions obtained in our study, we observed a declining trend for the SO/SO_2 ratio with the evolutionary stages of the low-mass star-forming region, which is just the opposite of that obtained by Herpin et al. (2009) and partially hinted from Fontani et al. (2023) for the high-mass star-forming region. The observed opposite trend between high-mass and low-mass cases arises due to several factors, such as density, temperature, envelope mass, and luminosity spatial resolutions. We need a large sample for both high-mass and low-mass cases with similar angular resolutions and sensitivity observations for statistical analysis. The column density ratio between SO_2 and SO is reported by Artur et al. (2023) as a function of bolometric temperature (T_{bol}) and bolometric luminosity (L_{bol}) of the PEACHES sample sources. They found no clear trend for SO/SO_2 as a function of T_{bol}. This ratio shows a tentative increasing trend for L_{bol} between 1 and $10L_{\odot}$ and for L_{bol} higher than $10L_{\odot}$, a tentative decreasing trend is seen for the SO/SO_2 ratio, which may be due to the photo-dissociation of SO_2 and enhancement of SO in those very luminous sources. However, in this work, a tentative trend in SO/SO_2 variation throughout various evolutionary phases of low-mass stars has been observed, providing systematic data for the first time for a small sample sources. Despite that, detailed investigations with a larger sample size are needed to confirm it. Nevertheless, analyzing a larger sample is beyond the scope of this work and will be addressed in future papers.

5.3 Chemical modeling

We use the three-phase (phase I → gas, phase II → icy grain surface, and phase III → homogeneous bulk ice mantle) Rokko code (Furuya et al., 2015; 2017) for the chemical modeling. A multilayer would form if more species are deposited than the available binding sites. Several monolayers of ice would build up during the evolution of grain. In the two-phase model, all the adsorbed materials are considered as the surface and are chemically reactive but indistinguishable. In the three-phase model, a distinction is made by considering the mantle and surface. All layers beneath the surface layers are considered the mantle, which is chemically unreactive. The surface layer is considered to be chemically active. In this work, we consider only the uppermost four monolayers as active ice layers; all the layers, including these active ice layers, are considered the bulk ice mantle. The gas and ice phase networks are adopted from Garrod (2013). We consider thermal desorption, photo-desorption, chemical desorption, and stochastic

TABLE 3 Derived rotational temperatures, column densities, and abundances (with respect to H_2) of SO, ^{34}SO, SO_2, and $^{34}SO_2$ in different stages of the low-mass star-formation process.

Source name	Stage of the source	Species	Rotational temperature (K)	Column density (cm^{-2})	Abundance of the species	Hydrogen column density $N(H_2)$ in cm^{-2}
L1544	PC	SO	⋯	$(2.03\pm0.07)\times10^{13}$	$(3.09\pm0.11)\times10^{-10}$	6.57×10^{22a} (Bizzocchi et al., 2013)
		^{34}SO	8.0	$(9.03\pm0.3)\times10^{11}$	$(1.38\pm0.05)\times10^{-11}$	
		SO_2	⋯	$(2.14\pm0.91)\times10^{12}$	$(3.26\pm1.39)\times10^{-11}$	
		$^{34}SO_2$	8.0	$(9.50\pm4.03)\times10^{10}$	$(1.45\pm0.61)\times10^{-12}$	
		OCS	8.0	$(4.21\pm0.3)\times10^{12}$	$(6.42\pm0.50)\times10^{-11}$	
		H_2S	10.0	$\geq1.6\times10^{12m}$	2.44×10^{-11}	
B1-b	FHSC	SO	⋯	$(2.43\pm0.02)\times10^{14}$	$(3.08\pm0.03)\times10^{-9}$	7.90×10^{22b} (Johnstone et al., 2010) Daniel et al. (2013)
		^{34}SO	$7.75^{+0.04}_{-0.04}$	$(1.08\pm0.01)\times10^{13}$	$(1.37\pm0.01)\times10^{-10}$	
		SO_2	⋯	$4.30^{+1.35}_{-1.13}\times10^{13}$	$5.44^{+1.71}_{-1.43}\times10^{-10}$	
		$^{34}SO_2$	$6.49^{+0.95}_{-0.74}$	$1.91^{+0.60}_{-0.50}\times10^{12}$	$2.42^{+0.76}_{-0.63}\times10^{-11}$	
		OCS	$14.5^{+0.42}_{-0.40}$	$(1.97\pm0.11)\times10^{13}$	$(2.5\pm0.14)\times10^{-10}$	
		H_2S	10.0	$(2.03\pm0.01)\times10^{13}$	$(2.57\pm0.01)\times10^{-10}$	
IRAS4A	Class 0	SO	⋯	$(2.24\pm0.03)\times10^{14}$	$(7.72\pm0.10)\times10^{-9}$	2.90×10^{22c} (López-Sepulcre et al., 2015)
		^{34}SO	9.22±0.06	$(9.95\pm0.14)\times10^{12}$	$(3.43\pm0.05)\times10^{-10}$	
		SO_2	⋯	$7.97^{+1.26}_{-1.10}\times10^{13}$	$2.75^{+0.43}_{-0.38}\times10^{-9}$	
		$_{34}SO_2$	$38.81^{+4.98}_{-3.96}$	$3.54^{+0.56}_{-0.48}\times10^{12}$	$1.22^{+0.19}_{-0.17}\times10^{-10}$	
		OCS	47.7±0.35	$(4.17\pm0.05)\times10^{13}$	$(1.4\pm0.02)\times10^{-9}$	
		H_2S	40.0	$(8.27\pm0.08)\times10^{13}$	$(2.85\pm0.03)\times10^{-9}$	
SVS13A	Class I	SO	⋯	$3.78^{+0.88}_{-0.70}\times10^{13}$	$2.63^{+0.88}_{-0.70}\times10^{-10}$	1.44×10^{23d} (Lefloch et al., 1998)
		$_{34}$SO	$35.47^{+6.34}_{-4.67}$	$1.68^{+0.39}_{-0.31}\times10^{12}$	$1.17^{+0.39}_{-0.31}\times10^{-11}$	
		SO_2	⋯	$(3.33\pm0.9)\times10^{13}$	$(2.31\pm0.9)\times10^{-10}$	
		$_{34}SO_2$	80	$(1.48\pm0.40)\times10^{12}$	$(1.03\pm0.40)\times10^{-11}$	
		OCS	$198.4^{+16.5}_{-14.1}$	$(3.69\pm0.14)\times10^{13}$	$(2.6\pm0.1)\times10^{-10}$	
		H_2S	80.0	$(4.28\pm0.01)\times10^{13}$	$(2.97\pm0.08)\times10^{-10}$	

[a]calculated for a beam size of 30″ with IRAM 30 m telescope.
[b]taking the average value from the two mentioned papers within 30″ IRAM beam.
[c]with a beam size of 30″
[d]scaled for 30″. We keep the excitation temperature fixed at 8 K for 34SO and $34SO_2$ in L1544 and assumed a fixed temperature of 80 K for $34SO_2$ in SVS13A [m] is taken from Vastel et al. (2018).

heating by cosmic rays (CRs). The chemical desorption of H_2S is important for the gas-phase abundances of S-bearing molecules. The chemical desorption probability of H_2S was determined to be 4% based on laboratory experiments (Oba et al., 2019; Furuya et al., 2022). The initial elemental abundances were used from Garrod (2013), which is originally based on the initial low metal elemental abundance set by Graedel et al. (1982), with the exception of He, C^+, N, and O values, which were obtained from their diffuse cloud model.

In an ideal scenario, it would be savvy to analyze how a molecular cloud evolves as it moves from the prestellar core stage to the Class I stage. However, for simplicity, we will limit our model to

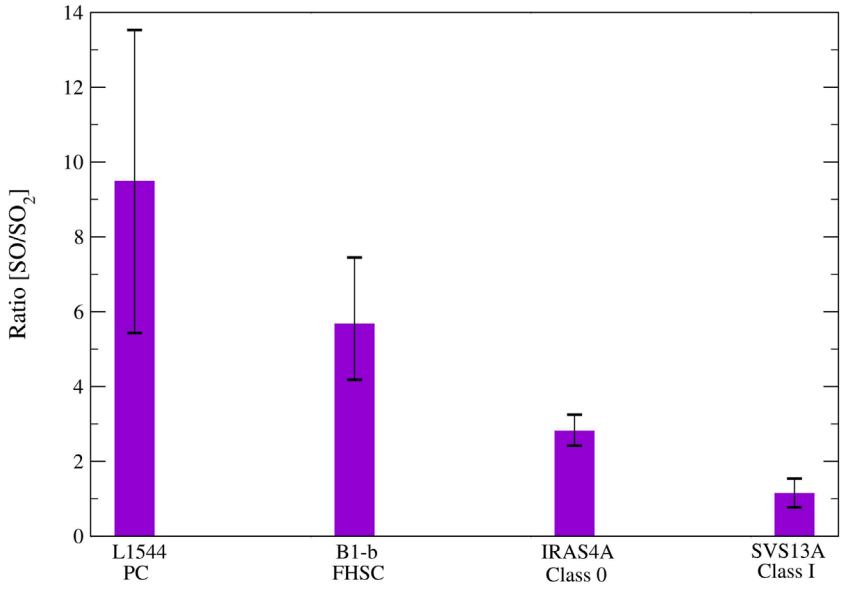

FIGURE 8
SO/SO_2 ratio in different evolutionary stages of the low-mass star-formation process.

the Class 0 stage. Here, we track the time evolution of both the inner portion and envelope of a cloud. Three stages are considered (see Figure 9): collapsing stage ($t_{coll} = 1 \times 10^6$ years), warm-up stage ($t_w = 2.85 \times 10^5$ years), and post-warm-up stage ($t_{pw} = 1 \times 10^5$ years). During the collapsing stage, the cloud is allowed to collapse from a minimum density ($\rho_{min} = 3 \times 10^3$ cm^{-3}) to a maximum density ($\rho_{max} = 10^7$ cm^{-3} for the inner portion and $\rho_{max} = 10^5$ cm^{-3} for the envelop). The visual extinction can increase from a minimum value of 2 mag to A_{Vmax} mag during this stage, as described by Garrod and Pauly (2011). The dust temperature is calculated based on the visual extinction parameter by the relation used in Garrod and Pauly (2011). The parameters we are considering illustrate a range of dust temperatures from 8 K to 16 K and a range of visual extinction from 2 mag to 446 mag during the collapsing stage of the inner region. For the envelop region, the dust temperature and visual extinction parameters are 8 K–16 K and 2 to 20 magnitudes, respectively. In the inner region of the warm-up stage, the temperature would increase to 400 K (50 K for the outer region) in $t_w = 2.85 \times 10^5$ years. In the warm-up stage, a good coupling between the gas and dust temperature is considered when the dust temperature increases beyond 10 K. During the warm-up stage, the density and visual extinction are kept constant at ρ_{max} and A_{Vmax}, respectively, but the temperature is allowed to increase up to a temperature T_{max} in t_w years. In the post-warm-up stage, density, temperature, and visual extinction are constant at ρ_{max}, T_{max}, and $A_{V_{max}}$, respectively.

Figures 10, 11 refer to the time evolution of SO and SO_2 and their ratio, respectively. The observed abundances shown in Figure 1 depict a sequential increasing trend from the prestellar core phase/first hydrostatic collapse phase (cold gas) to the Class 0 phase (warm gas). Our modeled abundances shown in Figure 10 show a similar trend. The horizontal lines mark the observed abundances. For the cold region (collapsing phase), the observed abundances of SO and SO_2 are taken from the abundances reported in Table 3 for L1544 and B1-b. For the warmer region (warm-up and post-warm-up stages), the abundances noted for the IRAS4A and SVS13A are highlighted. In the cold phase, the abundances of SO and SO_2 in the inner region (HC) match well with the observation at a time of 10^5 years, whereas for the outer region (ENV), it is 5×10^5 years. In the warm-up stage, the abundances overproduce SO and SO_2 for a temperature beyond 100 K. Conversely, the outer region underproduces the abundance. Our analysis reveals that in the inner section, particularly during the late warm-up and post-warm-up stages (>100 K), a significant amount of sulfur is present in the form of SO and SO_2. It is important to note that we initially assume an elemental sulfur abundance relative to H of 8×10^{-8} in our model, and our peak abundances (beyond the collapsing stage) of SO and SO_2 relative to H are 2.7×10^{-8} and 5.7×10^{-8}, respectively. This is not the case for the outer region.

In Figure 11demonstrates a decreasing trend from, the time evolution of SO/SO_2 is depicted. The observed abundance ratio between SO and SO_2 (see Figure 8) demonstrates a decreasing trend from cold gas to hot gas. This decreasing trend is similarly reflected in the modeled ratio depicted in Figure 11. Over time, density increases in the collapse stage, resulting in a steady declining trend of this ratio up to approximately 10^5 years for the inner region (HC) and approximately 5×10^5 years for the outer region (ENV). During the collapsing phase in the inner region (HC), the ratio of SO/SO_2 is significantly greater than 1. Between 100 and 300 K, the ratio is less than 1, but it is approximately 1 for temperatures exceeding 300 K, with a moderate warm-up time of 2.85×10^5. In the outer region (ENV), SO/SO_2 remains consistently greater than 1 throughout the period. Our observations, as presented in Figure 8, also revealed a SO/SO_2 ratio greater than 1 for all stages, indicating the proximity of the observed region to the envelop region examined in this study.

Drozdovskaya et al. (2018) carried out the large unbiased Protostellar Interferometric Line Survey (PILS) of IRAS 16293-2422

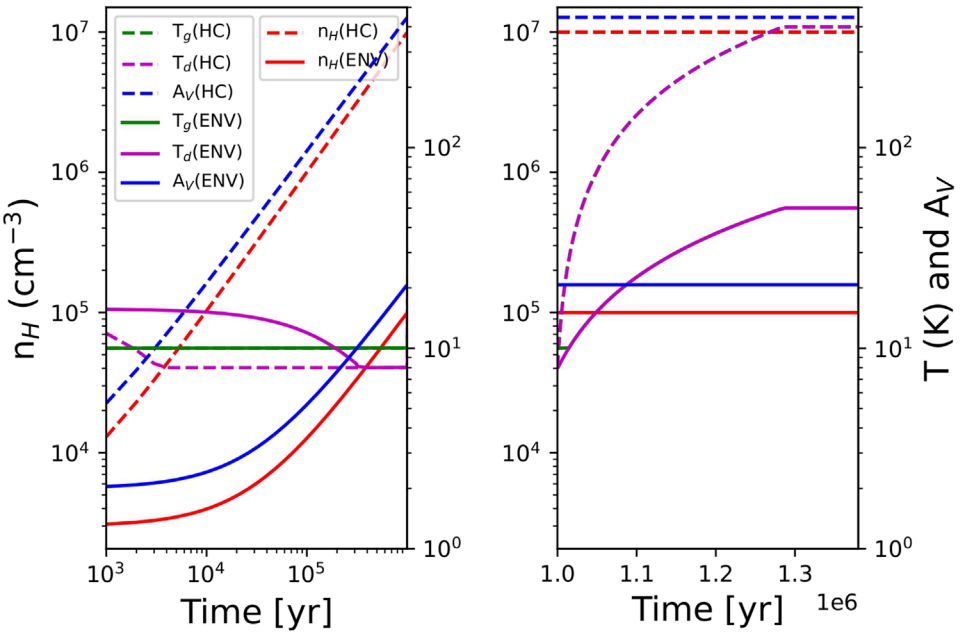

FIGURE 9
Time evolution of the physical parameters (density, temperature, and A_V) considered for the inner (HC) and envelop (ENV) regions is shown with dashed and solid curves, respectively.

with ALMA in the 329 – 363 GHz frequency range (Band 7) with a spectral resolution of 0.2 km s^{-1} and a beam size of 0.5″ (or 60 – 74 au in diameter, assuming a distance of 120 – 147 pc) to search for S-bearing molecules. They detected the SO_2 molecule in the $v = 0$ state based on 13 clean, non-blended lines at a column density of 1.5×10^{15} cm^{-2}, whereas they measured an upper limit of SO species in the same state with a value of 5.0×10^{14} cm^{-2}. They compared the SO/SO_2 ratio (~0.33) data with the 67P/C-G Comet and found that these two objects are in close agreement. Our model shows an SO/SO_2 ratio $\gg 1$ during the cold phase. In the late warm-up phase, it is <1 (100 – 300 K for the inner region). However, for temperatures exceeding 300 K, we observe it at approximately 1. This is possible because the data analyzed here obtained a rotational temperature for SO and SO_2 at 10 K and 44 K, respectively, for class 0 stage, suggesting the emission from different materials. In addition, our modeling suggests an SO/SO_2 ratio <1 at a much warmer region when compared to this observation.

6 Conclusion

We systematically investigated two primary sulfur-bearing species and their corresponding isotopologues by employing systematic data from the IRAM 30 m and astrochemical simulations. The major conclusions of this work are summarized as follows.

- In this study, we reported the detection of SO, SO_2, ^{34}SO, $^{34}SO_2$, OCS, and H_2S in four distinct phases of the low-mass star-formation process. Our analysis encompassed comprehensive line parameters for these molecules. Since SO and SO_2 are expected to be optically thick, we estimate their column density based on their isotopologues containing ^{34}S. The rotational diagram method or a simple LTE fitting was performed to determine their excitation temperature and column density. The abundances of SO, SO_2, OCS, and H_2S species exhibit an increase until the class 0 phase, followed by a decline in the class I stage.
- Our assessment extends to comparing the abundance of SO, SO_2, and their abundance ratio and outcomes derived from our models. This comparison, in turn, has facilitated the estimation of the temporal span of their abundances and the ratio of each phase. Observed SO and SO_2 abundances increase from cold to a hot gas, whereas the SO/SO_2 ratio decreases.
- Our model depicts that most sulfur is locked as SO and SO_2 when temperatures surpass 100 K. A notable contrast in the SO/SO_2 ratio between the inner and outer regions was obtained from our model. Within the inner region, the SO/SO_2 ratio is markedly higher than 1 at early times (8 – 16 K), declining to below 1 at intermediate times (100 – 300 K), and remaining at approximately 1 at later times (beyond 300 K). Our observations, depicted in Table 3; Figure 11, reveal a declining trend of the SO/SO_2 ratio across the evolutionary stages. Yet it remains greater than 1 at all stages. Given that our observations primarily capture low excitation transitions, they are focused on the intermediate region bridging the modeled inner and outer zones.

We note that additional observations of sample sources at various phases are required to obtain a trustworthy picture of

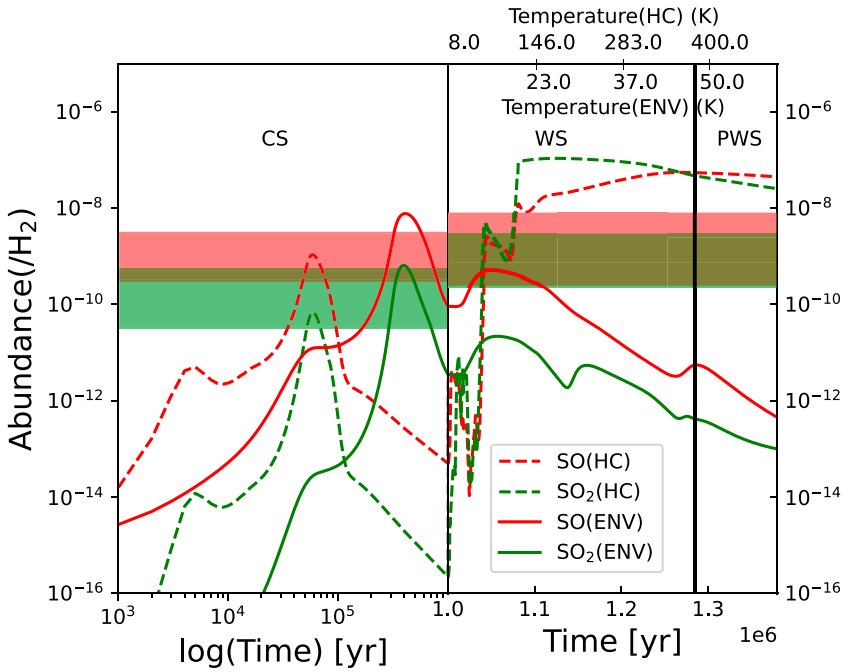

FIGURE 10
Time evolution of SO and SO_2 in the inner (HC) and outer (ENV) regions is represented by the dashed and solid curves, respectively. Various evolutionary stages (CS→ collapsing stage, WS→ warm-up stage, and PWS→ post-warm-up stage) are annotated on the graphs. The red and green shaded regions represent the observed abundances of SO and SO_2 in the cold (L1544 and B1-b) and the warm region (IRAS4A and SVS13A), respectively.

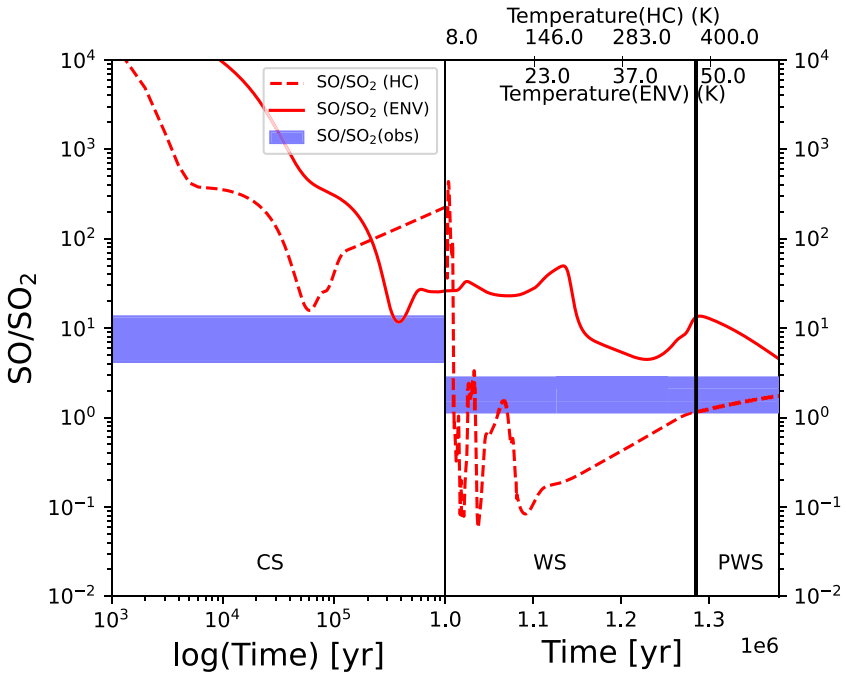

FIGURE 11
Time evolution of the SO/SO_2 ratio in the inner (HC) and outer (ENV) regions. Various evolutionary stages are **annotated** as given in Figure 1. The horizontal shaded region represents the observed abundances from Table 3 for the cold region (L1544 and B1b) and warm region (IRAS4A and SVS13A).

the chemical evolution throughout the solar-type star-formation process. This entails not just a significantly higher quantity of sources but also higher spatial and angular resolution to enable meaningful comparison across various evolutionary stages.

Data availability statement

Publicly available datasets were analyzed in this study. This data can be found here: We analyzed the ASAI data available in https://www.iram.fr/ILPA/LP007/. The CASSIS 503 software (https://cassis.irap.omp.eu/) was used for line analysis and for line identification.

Author contributions

RG: writing–original draft and writing–review and editing. AD: writing–original draft and writing–review and editing. PG: writing–original draft and writing–review and editing. SM: writing–original draft and writing–review and editing. KF: writing–original draft and writing–review and editing. KT: writing–original draft and writing–review and editing. TS: writing–original draft and writing–review and editing.

Funding

The author(s) declare that no financial support was received for the research, authorship, and/or publication of this article.

Acknowledgments

RG acknowledges the support from the Swami Vivekananda Merit-cum-Means Scholarship provided by the Government of West Bengal. AD is grateful for the assistance from the Centre for Astrochemical Studies (CAS) division at Max Planck Institute for Extraterrestrial Physics, Germany.

Conflict of interest

The authors declare that the research was conducted without any commercial or financial relationships that could potentially create a conflict of interest.

The author(s) declared that they were an editorial board member of Frontiers, at the time of submission. This had no impact on the peer review process and the final decision.

Publisher's note

References

Anglada, G., Rodríguez, L. F., and Torrelles, J. M. (2000). Discovery of a subarcsecond radio binary associated with the SVS 13 star in the HH 7-11 region. *Astrophysical J. Lett.* 542, L123–L126. doi:10.1086/312933

Artur, E., Guzmán, V. V., Jørgensen, J. K., Kristensen, L. E., Bergin, E. A., Harsono, D., et al. (2022). Physical properties of accretion shocks toward the Class I protostellar system Oph-IRS 44. *Astronomy Astrophysics* 667, A20. doi:10.1051/0004-6361/202244312

Artur, E., Guzmán, V. V., Yang, Y. L., Zhang, Y., and Sakai, N. (2023). The Perseus ALMA Chemical Survey (PEACHES). III. Sulfur-bearing species tracing accretion and ejection processes in young protostars. *Astronomy Astrophysics* 678, A124. doi:10.1051/0004-6361/202346728

Belloche, A., Maury, A. J., Maret, S., Anderl, S., Bacmann, A., André, P., et al. (2020). Questioning the spatial origin of complex organic molecules in young protostars with the CALYPSO survey. *Astronomy Astrophysics* 635, A198. doi:10.1051/0004-6361/201937352

Belov, S. P., Tretyakov, M. Y., Kozin, I. N., Klisch, E., Winnewisser, G., Lafferty, W. J., et al. (1998). High frequency transitions in the rotational spectrum of SO_2. *J. Mol. Spectrosc.* 191, 17–27. doi:10.1006/.jmsp.1998.7576

Belov, S. P., Yamada, K. M. T., Winnewisser, G., Poteau, L., Bocquet, R., Demaison, J., et al. (1995). Terahertz rotational spectrum of H_2S. *J. Mol. Spectrosc.* 173, 380–390. doi:10.1006/jmsp.1995.1242

Bhat, B., Kar, R., Mondal, S. K., Ghosh, R., Gorai, P., Shimonishi, T., et al. (2023). Chemical evolution of some selected complex organic molecules in low-mass star-forming regions. *Astrophysical J.* 958, 111. doi:10.3847/1538-4357/acfc4d

Bianchi, E., Codella, C., Ceccarelli, C., Vazart, F., Bachiller, R., Balucani, N., et al. (2019). The census of interstellar complex organic molecules in the Class I hot corino of SVS13-A. *Mon. Notices R. Astronomical Soc.* 483, 1850–1861. doi:10.1093/mnras/sty2915

Biver, N., Bockelee-Morvan, D., Colom, P., Crovisier, J., Davies, J. K., Dent, W. R. F., et al. (1997). Evolution of the outgassing of Comet Hale-Bopp (C/1995 O1) from radio observations. *Science* 275, 1915–1918. doi:10.1126/science.275.5308.1915

Bizzocchi, L., Caselli, P., Leonardo, E., and Dore, L. (2013). Detection of $^{15}NNH^+$ in L1544: non-LTE modelling of dyazenilium hyperfine line emission and accurate $^{14}N/^{15}N$ values. *Astronomy Astrophysics* 555, A109. doi:10.1051/.0004-6361/201321276

Blake, G. A., Sandell, G., van Dishoeck, E. F., Groesbeck, T. D., Mundy, L. G., and Aspin, C. (1995). A molecular line study of NGC 1333/IRAS 4. *Astrophysical J.* 441, 689. doi:10.1086/175392

Bogey, M., Civiš, S., Delcroix, B., Demuynck, C., Krupnov, A. F., Quiguer, J., et al. (1997). Microwave spectrum up to 900 GHz of SO created in highly excited states by electric discharge and UV-laser photolysis. *J. Mol. Spectrosc.* 182, 85–97. doi:10.1006/.jmsp.1996.7218

Boogert, A. C. A., Schutte, W. A., Helmich, F. P., Tielens, A. G. G. M., and Wooden, D. H. (1997). Infrared observations and laboratory simulations of interstellar CH_4_and SO_2_. *Astronomy Astrophysics* 317, 929–941.

Bottinelli, S., Ceccarelli, C., Lefloch, B., Williams, J. P., Castets, A., Caux, E., et al. (2004). Complex molecules in the hot core of the low-mass protostar NGC 1333 IRAS 4A. *Astrophysical J.* 615, 354–358. doi:10.1086/.423952

Bottinelli, S., Ceccarelli, C., Williams, J. P., and Lefloch, B. (2007). Hot corinos in NGC 1333-IRAS4B and IRAS2A. *Astronomy Astrophysics* 463, 601–610. doi:10.1051/.0004-6361:20065139

Buckle, J., and Fuller, G. (2003). Sulphur-bearing species as chemical clocks for low mass protostars? *A&* 399, 567–581. doi:10.1051/0004-6361:20021816

Caselli, P., Pineda, J. E., Sipilä, O., Zhao, B., Redaelli, E., Spezzano, S., et al. (2022). The Central 1000 au of a Prestellar Core Revealed with ALMA. II. Almost Complete Freeze-out. *Astrophysical J.* 929, 13. doi:10.3847/.1538-4357/ac5913

Caselli, P., Pineda, J. E., Zhao, B., Walmsley, M. C., Keto, E., Tafalla, M., et al. (2019). The Central 1000 au of a Pre-stellar Core Revealed with ALMA. I. 1.3 mm Continuum Observations. *Astrophysical J.* 874, 89. doi:10.3847/1538-4357/ab0700

Caux, E., Bottinelli, S., Vastel, C., and Glorian, J. M. (2011). "CASSIS, a software package to analyse high spectral resolution observations," in *The molecular universe*. Editors J. Cernicharo, and R. Bachiller, 280, 120.

Cazaux, S., Carrascosa, H., Muñoz Caro, G. M., Caselli, P., Fuente, A., Navarro-Almaida, D., et al. (2022). Photoprocessing of H_2S on dust grains. Building S chains in translucent clouds and comets. *Astronomy Astrophysics* 657, A100. doi:10.1051/0004-6361/202141861

Ceccarelli, C., Caselli, P., Fontani, F., Neri, R., López-Sepulcre, A., Codella, C., et al. (2017). Seeds Of Life In Space (SOLIS): The Organic Composition Diversity at 300-1000 au Scale in Solar-type Star-forming Regions. *Astrophysical J.* 850, 176. doi:10.3847/1538-4357/.aa961d

Cernicharo, J., and Guélin, M. (1987). The physical and chemical state of hcl2. *Astronomy Astrophysics* 176, 299–316.

Charnley, S. B. (1997). Chemical models of interstellar gas-grain processes - III. Molecular depletion in NGC 2024. *Mon. Notices R. Astronomical Soc.* 291, 455–460. doi:10.1093/mnras/291.3.455

Chen, X., Launhardt, R., and Henning, T. (2009). IRAM-PdBI observations of binary protostars. I. The hierarchical system SVS 13 in NGC 1333. *Astrophysical J.* 691, 1729–1737. doi:10.1088/0004-637X/691/2/.1729

Choi, M. (2005). Variability of the NGC 1333 IRAS 4A outflow: silicon monoxide observations. *Astrophysical J.* 630, 976–986. doi:10.1086/432113

Codella, C., Bachiller, R., and Reipurth, B. (1999). Low and high velocity SiO emission around young stellar objects. *Astronomy Astrophysics* 343, 585–598.

Codella, C., Bianchi, E., Podio, L., Mercimek, S., Ceccarelli, C., López-Sepulcre, A., et al. (2021). *The svs13-a class i chemical complexity as revealed by s-bearing species*. arXiv preprint arXiv:2109.01142.

Cox, E. G., Harris, R. J., Looney, L. W., Li, Z.-Y., Yang, H., Tobin, J. J., et al. (2018). ALMA's polarized view of 10 protostars in the Perseus molecular cloud. *Astrophysical J.* 855, 92. doi:10.3847/1538-4357/aaacd2

Crapsi, A., Caselli, P., Walmsley, M. C., and Tafalla, M. (2007). Observing the gas temperature drop in the high-density nucleus of L 1544. *Astronomy Astrophysics* 470, 221–230. doi:10.1051/0004-6361:20077613

Daniel, F., Gérin, M., Roueff, E., Cernicharo, J., Marcelino, N., Lique, F., et al. (2013). Nitrogen isotopic ratios in barnard 1: a consistent study of the n2h+, nh3, cn, hcn, and hnc isotopologues. *A&* 560, A3. doi:10.1051/0004-6361/201321939

De Simone, M., Codella, C., Ceccarelli, C., López-Sepulcre, A., Witzel, A., Neri, R., et al. (2020). Seeds of Life in Space (SOLIS). X. Interstellar complex organic molecules in the NGC 1333 IRAS 4A outflows. *astronomy astrophysics* 640, A75. doi:10.1051/0004-6361/201937004

De Simone, M., Codella, C., Testi, L., Belloche, A., Maury, A. J., Anderl, S., et al. (2017). Glycolaldehyde in Perseus young solar analogs. *Astronomy Astrophysics* 599, A121. doi:10.1051/0004-6361/201630049

Diaz-Rodriguez, A. K., Anglada, G., Blázquez-Calero, G., Osorio, M., Gómez, J. F., Fuller, G. A., et al. (2022). The physical properties of the svs 13 protobinary system: two circumstellar disks and a spiraling circumbinary disk in the making. *ApJ* 930, 91. doi:10.3847/1538-4357/ac3b50

Dionatos, O., Kristensen, L. E., Tafalla, M., Güdel, M., and Persson, M. (2020). Feedback of molecular outflows from protostars in NGC 1333 revealed by Herschel and Spitzer spectro-imaging observations. *Astronomy Astrophysics* 641, A36. doi:10.1051/0004-6361/202037684

Drozdovskaya, M. N., van Dishoeck, E. F., Jørgensen, J. K., Calmonte, U., van der Wiel, M. H. D., Coutens, A., et al. (2018). The ALMA-PILS survey: the sulphur connection between protostars and comets: IRAS 16293-2422 B and 67P/Churyumov-Gerasimenko. *Mon. Notices R. Astronomical Soc.* 476, 4949–4964. doi:10.1093/mnras/.sty462

Esplugues, G. B., Viti, S., Goicoechea, J. R., and Cernicharo, J. (2014). Modelling the sulphur chemistry evolution in Orion KL. *Astronomy Astrophysics* 567, A95. doi:10.1051/0004-6361/201323010

Fegley, B. (1999). Chemical and physical processing of presolar materials in the solar nebula and the implications for preservation of presolar materials in comets. *Space Sci. Rev.* 90, 239–252. doi:10.1007/978-94-011-4211-3_22

Fontani, F., Roueff, E., Colzi, L., and Caselli, P. (2023). The evolution of sulphur-bearing molecules in high-mass star-forming cores. *Astronomy Astrophysics* 680, A58. doi:10.1051/0004-6361/202347565

Fuente, A., Cernicharo, J., Roueff, E., Gerin, M., Pety, J., Marcelino, N., et al. (2016). Ionization fraction and the enhanced sulfur chemistry in Barnard 1. *Astronomy Astrophysics* 593, A94. doi:10.1051/0004-6361/201628285

Fuente, A., Rivière-Marichalar, P., Beitia-Antero, L., Caselli, P., Wakelam, V., Esplugues, G., et al. (2023). Gas phase Elemental abundances in Molecular cloudS (GEMS). VII. Sulfur elemental abundance. *Astronomy Astrophysics* 670, A114. doi:10.1051/0004-6361/202244843

Furuya, K., Aikawa, Y., Hincelin, U., Hassel, G. E., Bergin, E. A., Vasyunin, A. I., et al. (2015). Water deuteration and ortho-to-para nuclear spin ratio of H_2 in molecular clouds formed via the accumulation of H I gas. *Astronomy Astrophysics* 584, A124. doi:10.1051/0004-6361/201527050

Furuya, K., Drozdovskaya, M. N., Visser, R., van Dishoeck, E. F., Walsh, C., Harsono, D., et al. (2017). Water delivery from cores to disks: deuteration as a probe of the prestellar inheritance of H_2O. *Astronomy Astrophysics* 599, A40. doi:10.1051/0004-6361/201629269

Furuya, K., Oba, Y., and Shimonishi, T. (2022). Quantifying the chemical desorption of H_2S and PH_3 from amorphous water-ice surfaces. *Astrophysical J.* 926, 171. doi:10.3847/1538-4357/ac4260

García-Rojas, J., Esteban, C., Peimbert, M., Costado, M., Rodríguez, M., Peimbert, A., et al. (2006). Faint emission lines in the galactic h ii regions m16, m20 and ngc 3603. *MNRAS* 368, 253–279. doi:10.1111/j.1365-2966.2006.10105.x

Garrod, R. T. (2013). A three-phase chemical model of hot cores: the formation of Glycine. *Astrophysical J.* 765, 60. doi:10.1088/0004-637X/765/1/60

Garrod, R. T., and Pauly, T. (2011). On the formation of co2 and other interstellar ices. *ApJ* 735, 15. doi:10.1088/.0004-637X/735/1/15

Gerin, M., Pety, J., Commercon, B., Fuente, A., Cernicharo, J., Marcelino, N., et al. (2017). Evidence for disks at an early stage in class 0 protostars? *A&* 606, A35. doi:10.1051/0004-6361/201630187

Goldsmith, P. F., and Langer, W. D. (1999). Population diagram analysis of molecular line emission. *Astrophysical J.* 517, 209–225. doi:10.1086/307195

Gorai, P., Das, A., Das, A., Sivaraman, B., Etim, E. E., and Chakrabarti, S. K. (2017). A search for interstellar monohydric thiols. *Astrophysical J.* 836, 70. doi:10.3847/1538-4357/836/1/70

Graedel, T. E., Langer, W. D., and Frerking, M. A. (1982). The kinetic chemistry of dense interstellar clouds. *apjs* 48, 321–368. doi:10.1086/190780

Harsono, D., Jørgensen, J. K., van Dishoeck, E. F., Hogerheijde, M. R., Bruderer, S., Persson, M. V., et al. (2014). Rotationally-supported disks around Class I sources in Taurus: disk formation constraints. *Astronomy Astrophysics* 562, A77. doi:10.1051/0004-6361/201322646

Hatchell, J., Fuller, G. A., and Richer, J. S. (2007). Star formation in Perseus. III. Outflows. *Astronomy Astrophysics* 472, 187–198. doi:10.1051/0004-6361:20066467

Hatchell, J., Richer, J. S., Fuller, G. A., Qualtrough, C. J., Ladd, E. F., and Chandler, C. J. (2005). Star formation in Perseus. Clusters, filaments and the conditions for star formation. *Astronomy Astrophysics* 440, 151–161. doi:10.1051/0004-6361:20041836

Hatchell, J., Thompson, M. A., Millar, T. J., and MacDonald, G. H. (1998). Sulphur chemistry and evolution in hot cores. *Astronomy Astrophysics* 338, 713–722.

Herpin, F., Marseille, M., Wakelam, V., Bontemps, S., and Lis, D. C. (2009). S-bearing molecules in massive dense cores. *Astronomy Astrophysics* 504, 853–867. doi:10.1051/0004-6361/200811257

Hirota, T., Bushimata, T., Choi, Y. K., Honma, M., Imai, H., Iwadate, K., et al. (2008). Astrometry of H_2O masers in nearby star-forming regions with VERA. *II. SVS13 NGC1333. Publ. ASJ* 60, 37–44. doi:10.1093/pasj/.60.1.37

Holdship, J., Viti, S., Jimenez-Serra, I., Lefloch, B., Codella, C., Podio, L., et al. (2016). H_2S in the L1157-B1 bow shock. *Mon. Notices R. Astronomical Soc.* 463, 802–810. doi:10.1093/mnras/stw1977

Hsieh, T. H., Pineda, J. E., Segura-Cox, D. M., Caselli, P., Valdivia-Mena, M. T., Gieser, C., et al. (2024). PRODIGE – envelope to Disk with NOEMA III. The origin of complex organic molecule emission in SVS13A. *arXiv e-prints arXiv:2403.16892* 686, A289. doi:10.1051/0004-6361/202449417

Huang, Y.-H., and Hirano, N. (2013). Probing the earliest stage of protostellar evolution—barnard 1-bN and barnard 1-bS. *Astrophysical J.* 766, 131. doi:10.1088/.0004-637X/766/2/131

Jenkins, E. B. (2009). A unified representation of gas-phase element depletions in the interstellar medium. *Astrophysical J.* 700, 1299–1348. doi:10.1088/.0004-637X/700/2/1299

Jiménez-Escobar, A., Muñoz Caro, G. M., Ciaravella, A., Cecchi-Pestellini, C., Candia, R., and Micela, G. (2012). Soft X-ray irradiation of H_2S ice and the presence of S_2 in comets. *Astrophysical J. Lett.* 751, L40. doi:10.1088/2041-8205/751/2/L40

Johnstone, D., Rosolowsky, E., Tafalla, M., and Kirk, H. (2010). Dense gas tracers in Perseus: relating the N_2H^+, NH_3, and dust continuum properties of pre- and protostellar cores. *Astrophysical J.* 711, 655–670. doi:10.1088/0004-637X/711/2/655

Jørgensen, J. K., Schöier, F. L., and van Dishoeck, E. F. (2004). Molecular inventories and chemical evolution of low-mass protostellar envelopes. *Astronomy Astrophysics* 416, 603–622. doi:10.1051/0004-6361:20034440

Karska, A., Herczeg, G. J., van Dishoeck, E. F., Wampfler, S. F., Kristensen, L. E., Goicoechea, J. R., et al. (2013). Water in star-forming regions with*Herschel*(WISH): III. Far-infrared cooling lines in low-mass young stellar objects⋆. *Astronomy Astrophysics* 552, A141. doi:10.1051/.0004-6361/201220028

Keto, E., and Caselli, P. (2010). Dynamics and depletion in thermally supercritical starless cores. *MNRAS* 402, 1625–1634. doi:10.1111/j.1365-2966.2009.16033.x

Klaus, T., Saleck, A. H., Belov, S. P., Winnewisser, G., Hirahara, Y., Hayashi, M., et al. (1996). Pure rotational spectra of SO: rare isotopomers in the 80-GHz to 1.1-THz region. *J. Mol. Spectrosc.* 180, 197–206. doi:10.1006/jmsp.1996.0243

Kolesniková, L., Tercero, B., Cernicharo, J., Alonso, J. L., Daly, A. M., Gordon, B. P., et al. (2014). Spectroscopic characterization and detection of ethyl mercaptan in orion. *Astrophysical J. Lett.* 784, L7. doi:10.1088/.2041-8205/784/1/L7

Kristensen, L. E., van Dishoeck, E. F., Bergin, E. A., Visser, R., Yıldız, U. A., San Jose-Garcia, I., et al. (2012). Water in star-forming regions with Herschel (WISH). II. Evolution of 557 GHz 1_{10}-1_{01} emission in low-mass protostars. *Astronomy Astrophysics* 542, A8. doi:10.1051/0004-6361/201118146

Laas, J. C., and Caselli, P. (2019). Modeling sulfur depletion in interstellar clouds. *Astronomy Astrophysics* 624, A108. doi:10.1051/0004-6361/201834446

Larson, R. B. (1969). Numerical calculations of the dynamics of a collapsing proto-star ∗ . *Mon. Notices R. Astronomical Soc.* 145, 271–295. doi:10.1093/mnras/145.3.271

Lefèvre, C., Cabrit, S., Maury, A. J., Gueth, F., Tabone, B., Podio, L., et al. (2017). CALYPSO view of SVS 13A with PdBI: multiple jet sources. *Astronomy Astrophysics* 604, L1. doi:10.1051/0004-6361/201730766

Lefloch, B., Bachiller, R., Ceccarelli, C., Cernicharo, J., Codella, C., Fuente, A., et al. (2018). Astrochemical evolution along star formation: overview of the IRAM Large Program ASAI. *Mon. Notices R. Astronomical Soc.* 477, 4792–4809. doi:10.1093/mnras/sty937

Lefloch, B., Castets, A., Cernicharo, J., Langer, W. D., and Zylka, R. (1998). Cores and cavities in NGC 1333. *Astronomy Astrophysics* 334, 269–279.

Lodders, K. (2003). Solar system abundances and condensation temperatures of the elements. *apj* 591, 1220–1247. doi:10.1086/375492

Loison, J.-C., Wakelam, V., Gratier, P., Hickson, K. M., Bacmann, A., Agúndez, M., et al. (2019). Oxygen fractionation in dense molecular clouds. *Mon. Notices R. Astronomical Soc.* 485, 5777–5789. doi:10.1093/.mnras/stz560

Looney, L. W., Mundy, L. G., and Welch, W. J. (2000). Unveiling the circumstellar envelope and disk: a subarcsecond survey of circumstellar structures. *Astrophysical J.* 529, 477–498. doi:10.1086/308239

López-Sepulcre, A., Jaber, A. A., Mendoza, E., Lefloch, B., Ceccarelli, C., Vastel, C., et al. (2015). Shedding light on the formation of the pre-biotic molecule formamide with ASAI. *Mon. Notices R. Astronomical Soc.* 449, 2438–2458. doi:10.1093/mnras/stv377

López-Sepulcre, A., Sakai, N., Neri, R., Imai, M., Oya, Y., Ceccarelli, C., et al. (2017). Complex organics in IRAS 4A revisited with ALMA and PdBI: striking contrast between two neighbouring protostellar cores. *Astronomy Astrophysics* 606, A121. doi:10.1051/0004-6361/201630334

Mandeville, C. W. (2010). Sulfur: a ubiquitous and useful tracer in earth and planetary sciences. *Elements* 6, 75–80. doi:10.2113/gselements.6.2.75

Marcelino, N., Agúndez, M., Cernicharo, J., Roueff, E., and Tafalla, M. (2018). Discovery of the elusive radical NCO and confirmation of H_2NCO^+ in space. *Astronomy Astrophysics* 612, L10. doi:10.1051/0004-6361/201833074

Martín-Hernández, N. L., Peeters, E., Morisset, C., Tielens, A. G. G. M., Cox, P., Roelfsema, P. R., et al. (2002). ISO spectroscopy of compact H II regions in the Galaxy. II. Ionization and elemental abundances. *Astronomy Astrophysics* 381, 606–627. doi:10.1051/0004-6361:20011504

McGuire, B. A. (2022). 2021 census of interstellar, circumstellar, extragalactic, protoplanetary disk, and exoplanetary molecules. *Astrophysical J. Suppl.* 259, 30. doi:10.3847/.1538-4365/ac2a48

Müller, H. S. P., Schlöder, F., Stutzki, J., and Winnewisser, G. (2005). The Cologne Database for Molecular Spectroscopy, CDMS: a useful tool for astronomers and spectroscopists. *J. Mol. Struct.* 742, 215–227. doi:10.1016/j.molstruc.2005.01.027

Navarro-Almaida, D., Le Gal, R., Fuente, A., Rivière-Marichalar, P., Wakelam, V., Cazaux, S., et al. (2020). Gas phase Elemental abundances in Molecular cloudS (GEMS). II. On the quest for the sulphur reservoir in molecular clouds: the H_2S case. *Astronomy Astrophysics* 637, A39. doi:10.1051/0004-6361/201937180

Oba, Y., Tomaru, T., Kouchi, A., and Watanabe, N. (2019). Physico-chemical behavior of hydrogen sulfide induced by reactions with H and D atoms on different types of ice surfaces at low temperature. *Astrophysical J.* 874, 124. doi:10.3847/1538-4357/ab0961

Ospina-Zamudio, J., Lefloch, B., Ceccarelli, C., Kahane, C., Favre, C., López-Sepulcre, A., et al. (2018). First hot corino detected around an isolated intermediate-mass protostar: cep E-mm. *Astronomy Astrophysics* 618, A145. doi:10.1051/0004-6361/201832857

Oya, Y., López-Sepulcre, A., Sakai, N., Watanabe, Y., Higuchi, A. E., Hirota, T., et al. (2019). Sulfur-bearing species tracing the disk/envelope system in the class I protostellar source elias 29. *Astrophysical J.* 881, 112. doi:10.3847/1538-4357/ab2b97

Palumbo, M. E., Tielens, A. G. G. M., and Tokunaga, A. T. (1995). Solid carbonyl sulphide (OCS) in W33A. *Astrophysical J.* 449, 674. doi:10.1086/176088

Pasek, M. A., Milsom, J. A., Ciesla, F. J., Lauretta, D. S., Sharp, C. M., and Lunine, J. I. (2005). Sulfur chemistry with time-varying oxygen abundance during Solar System formation. *Icarus* 175, 1–14. doi:10.1016/j.icarus.2004.10.012

Pezzuto, S., Elia, D., Schisano, E., Strafella, F., Di Francesco, J., Sadavoy, S., et al. (2012). Herschel observations of B1-bS and B1-bN: two first hydrostatic core candidates in the Perseus star-forming cloud. *Astronomy Astrophysics* 547, A54. doi:10.1051/0004-6361/201219501

Podio, L., Lefloch, B., Ceccarelli, C., Codella, C., and Bachiller, R. (2014). Molecular ions in the protostellar shock L1157-B1. *Astronomy Astrophysics* 565, A64. doi:10.1051/0004-6361/201322928

Rivière-Marichalar, P., Fuente, A., Goicoechea, J. R., Pety, J., Le Gal, R., Gratier, P., et al. (2019). Abundances of sulphur molecules in the Horsehead nebula. First NS^+ detection in a photodissociation region. *Astronomy Astrophysics* 628, A16. doi:10.1051/0004-6361/201935354

Rocha, W. R. M., van Dishoeck, E. F., Ressler, M. E., van Gelder, M. L., Slavicinska, K., Brunken, N. G. C., et al. (2024). JWST Observations of Young protoStars (JOYS+): detecting icy complex organic molecules and ions. I. CH_4, SO_2, $HCOO^-$, OCN^-, H_2CO, HCOOH, CH_3CH_2OH, CH_3CHO, CH_3OCHO, and CH_3COOH. *Astronomy Astrophysics* 683, A124. doi:10.1051/0004-6361/202348427

Sakai, N., Sakai, T., Hirota, T., Watanabe, Y., Ceccarelli, C., Kahane, C., et al. (2014). Change in the chemical composition of infalling gas forming a disk around a protostar. *nature* 507, 78–80. doi:10.1038/nature13000

Santangelo, G., Codella, C., Cabrit, S., Maury, A. J., Gueth, F., Maret, S., et al. (2015). Jet multiplicity in the proto-binary system NGC 1333-IRAS4A: the detailed CALYPSO IRAM-PdBI view⋆⋆⋆. *Astronomy Astrophysics* 584, A126. doi:10.1051/0004-6361/201526323

Santangelo, G., Nisini, B., Codella, C., Lorenzani, A., Yıldız, U. A., Antoniucci, S., et al. (2014). Water distribution in shocked regions of the NGC 1333-IRAS 4A protostellar outflow. *Astronomy Astrophysics* 568, A125. doi:10.1051/0004-6361/201424034

Shimonishi, T., Onaka, T., Kawamura, A., and Aikawa, Y. (2016). The detection of a hot molecular core in the large magellanic cloud with ALMA. *Astrophysical J.* 827, 72. doi:10.3847/0004-637X/827/1/72

Shimonishi, T., Tanaka, K. E. I., Zhang, Y., and Furuya, K. (2023). The detection of hot molecular cores in the small magellanic cloud. *Astrophysical J. Lett.* 946, L41. doi:10.3847/2041-8213/acc031

Shimonishi, T., Watanabe, Y., Nishimura, Y., Aikawa, Y., Yamamoto, S., Onaka, T., et al. (2018). A multiline study of a high-mass young stellar object in the small magellanic cloud with ALMA: the detection of methanol gas at 0.2 solar metallicity. *Astrophysical J.* 862, 102. doi:10.3847/1538-4357/aacd0c

Shingledecker, C. N., Lamberts, T., Laas, J. C., Vasyunin, A., Herbst, E., Kästner, J., et al. (2020). Efficient production of S_8 in interstellar ices: the effects of cosmic-ray-driven radiation chemistry and nondiffusive bulk reactions. *Astrophysical J.* 888, 52. doi:10.3847/1538-4357/ab5360

Smith, R. G. (1991). A search for solid H_2S in dense clouds. *Mon. Notices R. Astronomical Soc.* 249, 172–176. doi:10.1093/mnras/249.1.172

Spezzano, S., Caselli, P., Bizzocchi, L., Giuliano, B. M., and Lattanzi, V. (2017). The observed chemical structure of L1544. *Astronomy Astrophysics* 606, A82. doi:10.1051/.0004-6361/201731262

Sutton, E. C., Peng, R., Danchi, W. C., Jaminet, P. A., Sandell, G., and Russell, A. P. G. (1995). The distribution of molecules in the core of OMC-1. *Astrophysical J.* 97, 455. doi:10.1086/192147

Tafalla, M., Mardones, D., Myers, P. C., Caselli, P., Bachiller, R., and Benson, P. J. (1998). L1544: a starless dense core with extended inward motions. *Astrophysical J.* 504, 900–914. doi:10.1086/306115

Taquet, V., Codella, C., De Simone, M., López-Sepulcre, A., Pineda, J. E., Segura-Cox, D., et al. (2020). Seeds of Life in Space (SOLIS). VI. Chemical evolution of sulfuretted species along the outflows driven by the low-mass protostellar binary NGC 1333-IRAS4A. *Astronomy Astrophysics* 637, A63. doi:10.1051/0004-6361/201937072

Taquet, V., López-Sepulcre, A., Ceccarelli, C., Neri, R., Kahane, C., and Charnley, S. B. (2015). Constraining the abundances of complex organics in the inner regions of solar-type protostars. *Astrophysical J.* 804, 81. doi:10.1088/0004-637X/804/2/81

Tieftrunk, A., Pineau des Forets, G., Schilke, P., and Walmsley, C. M. (1994). SO and H_2_S in low density molecular clouds. *Astronomy Astrophysics* 289, 579–596.

Tobin, J. J., Looney, L. W., Li, Z.-Y., Chandler, C. J., Dunham, M. M., Segura-Cox, D., et al. (2016). The VLA nascent disk and multiplicity survey of Perseus protostars (VANDAM). II. Multiplicity of protostars in the Perseus molecular cloud. *Astrophysical J.* 818, 73. doi:10.3847/0004-637X/818/1/73

Tobin, J. J., Looney, L. W., Li, Z.-Y., Sadavoy, S. I., Dunham, M. M., Segura-Cox, D., et al. (2018). The VLA/ALMA nascent disk and multiplicity (VANDAM) survey of Perseus protostars. VI. Characterizing the formation mechanism for close multiple systems. *Astrophysical J.* 867, 43. doi:10.3847/1538-4357/.aae1f7

Tychoniec, Ł., van Dishoeck, E. F., van't Hoff, M. L. R., van Gelder, M. L., Tabone, B., Chen, Y., et al. (2021). Which molecule traces what: chemical diagnostics of protostellar sources. *Astronomy Astrophysics* 655, A65. doi:10.1051/.0004-6361/202140692

van der Tak, F. F. S., Boonman, A. M. S., Braakman, R., and van Dishoeck, E. F. (2003). "Sulphur chemistry in the envelopes of massive young stars," in *SFChem 2002: chemistry as a diagnostic of star formation*. Editors C. L. Curry, and M. Fich, 437. doi:10.48550/arXiv.astro-ph/.0212325

Vastel, C., Ceccarelli, C., Lefloch, B., and Bachiller, R. (2014). The origin of complex organic molecules in prestellar cores. *Astrophysical J.* 795, L2. doi:10.1088/2041-8205/795/1/L2

Vastel, C., Quénard, D., Le Gal, R., Wakelam, V., Andrianasolo, A., Caselli, P., et al. (2018). Sulphur chemistry in the L1544 pre-stellar core. *Mon. Notices R. Astronomical Soc.* 478, 5514–5532. doi:10.1093/.mnras/sty1336

Wakelam, V., Caselli, P., Ceccarelli, C., Herbst, E., and Castets, A. (2004). Resetting chemical clocks of hot cores based on S-bearing molecules. *Astronomy Astrophysics* 422, 159–169. doi:10.1051/0004-6361:20047186

Wakelam, V., Hersant, F., and Herpin, F. (2011). Sulfur chemistry: 1D modeling in massive dense cores. *Astronomy Astrophysics* 529, A112. doi:10.1051/.0004-6361/201016164

Winton, R. S., and Gordy, W. (1970). High-precision millimeter-wave spectroscopy with the lamb dip. *Phys. Lett. A* 32, 219–220. doi:10.1016/0375-9601(70)90287-2

Woodney, L. M., A'Hearn, M. F., McMullin, J., and Samarasinha, N. (1997). Sulfur chemistry at millimeter wavelengths in C/Hale-Bopp. *Earth Moon Planets* 78, 69–70. doi:10.1023/A:1006275412491

Yamamoto, S. (2017). *Introduction to astrochemistry: chemical evolution from interstellar clouds to star and planet formation*. Springer.

Yan, Y. T., Henkel, C., Kobayashi, C., Menten, K. M., Gong, Y., Zhang, J. S., et al. (2023). Direct measurements of carbon and sulfur isotope ratios in the Milky Way. *Astronomy Astrophysics* 670, A98. doi:10.1051/.0004-6361/202244584

Yang, Y.-L., Sakai, N., Zhang, Y., Murillo, N. M., Zhang, Z. E., Higuchi, A. E., et al. (2021). The Perseus ALMA chemistry survey (PEACHES). I. The complex organic molecules in Perseus embedded protostars. *Astrophysical J.* 910, 20. doi:10.3847/1538-4357/.abdfd6

Yıldız, U. A., Kristensen, L. E., van Dishoeck, E. F., Belloche, A., van Kempen, T. A., Hogerheijde, M. R., et al. (2012). APEX-CHAMP$^+$ high-J CO observations of low-mass young stellar objects. III. NGC 1333 IRAS 4A/4B envelope, outflow, and ultraviolet heating. *Astronomy Astrophysics* 542, A86. doi:10.1051/0004-6361/201118368

Zhang, Z. E., Yang, Y.-l., Zhang, Y., Cox, E. G., Zeng, S., Murillo, N. M., et al. (2023). The Perseus ALMA chemistry survey (PEACHES). II. Sulfur-Bearing species and dust polarization revealing shocked regions in protostars in the Perseus molecular cloud. *Astrophysical J.* 946, 113. doi:10.3847/1538-4357/acbdf7

Zucker, C., Schlafly, E. F., Speagle, J. S., Green, G. M., Portillo, S. K. N., Finkbeiner, D. P., et al. (2018). Mapping distances across the Perseus molecular cloud using CO observations, stellar photometry, and Gaia DR2 parallax measurements. *Astrophysical J.* 869, 83. doi:10.3847/1538-4357/aae97c